Physics & Astronomy Faculty Works

Physics & Astronomy

5-11-2016

KELT-14b And KELT-15b: An Independent Discovery Of WASP-122b And A New Hot Jupiter

J. E. Rodriguez

K. D. Colón

K. G. Stassun

D. Wright

P. A. Cargile

See next page for additional authors

Follow this and additional works at: http://works.swarthmore.edu/fac-physics

Part of the Astrophysics and Astronomy Commons

Authors

J. E. Rodriguez, K. D. Colón, K. G. Stassun, D. Wright, P. A. Cargile, D. Bayliss, J. Pepper, K. A. Collins, R. B. Kuhn, M. B. Lund, R. J. Siverd, G. Zhou, B. S. Gaudi, C. G. Tinney, K. Penev, T. G. Tan, C. Stockdale, I. A. Curtis, D. James, S. Udry, D. Segransan, A. Bieryla, D. W. Latham, T. G. Beatty, J. D. Eastman, G. Myers, J. Bartz, J. Bento, Eric L.N. Jensen, T. E. Oberst, and D. J. Stevens

KELT-14b AND KELT-15b: AN INDEPENDENT DISCOVERY OF WASP-122b AND A NEW HOT JUPITER

Joseph E. Rodriguez[1], Knicole D. Colón[2,3], Keivan G. Stassun[1,4], Duncan Wright[5,6], Phillip A. Cargile[7],
Daniel Bayliss[8], Joshua Pepper[9], Karen A. Collins[1], Rudolf B. Kuhn[10], Michael B. Lund[1], Robert J. Siverd[11],
George Zhou[7,12], B. Scott Gaudi[13], C. G. Tinney[5,6], Kaloyan Penev[14], T. G. Tan[15], Chris Stockdale[16,17],
Ivan A. Curtis[18], David James[19], Stephane Udry[8], Damien Segransan[8], Allyson Bieryla[7], David W. Latham[7],
Thomas G. Beatty[20,21], Jason D. Eastman[7], Gordon Myers[16,22], Jonathan Bartz[9], Joao Bento[12], Eric L. N. Jensen[23],
Thomas E. Oberst[24], and Daniel J. Stevens[13]

[1] Department of Physics and Astronomy, Vanderbilt University, 6301 Stevenson Center, Nashville, TN 37235, USA
[2] NASA Ames Research Center, M/S 244-30, Moffett Field, CA 94035, USA
[3] Bay Area Environmental Research Institute, 625 2nd St. Ste 209 Petaluma, CA 94952, USA
[4] Department of Physics, Fisk University, 1000 17th Avenue North, Nashville, TN 37208, USA
[5] School of Physics, UNSW Australia, 2052, Australia
[6] Australian Centre for Astrobiology, UNSW Australia, 2052, Australia
[7] Harvard-Smithsonian Center for Astrophysics, 60 Garden St., Cambridge, MA 02138, USA
[8] Observatoire Astronomique de l'Université de Genève, Chemin des Maillettes 51, 1290 Sauverny, Switzerland
[9] Department of Physics, Lehigh University, 16 Memorial Drive East, Bethlehem, PA 18015, USA
[10] South African Astronomical Observatory, P.O. Box 9, Observatory 7935, South Africa
[11] Las Cumbres Observatory Global Telescope Network, 6740 Cortona Dr., Suite 102, Santa Barbara, CA 93117, USA
[12] Research School of Astronomy and Astrophysics, Australian National University, Canberra, ACT 2611, Australia
[13] Department of Astronomy, The Ohio State University, Columbus, OH 43210, USA
[14] Department of Astrophysical Sciences, Princeton University, Princeton, NJ 08544, USA
[15] Perth Exoplanet Survey Telescope, Perth, Australia
[16] American Association of Variable Star Observers, 49 Bay State Rd., Cambridge, MA 02138, USA
[17] Hazelwood Observatory, Australia
[18] IAU Minor Planet Center Observatory Code D79, Vale Park, Adelaide, South Australia
[19] Cerro Tololo InterAmerican Observatory, Casilla 603, La Serena, Chile
[20] Department of Astronomy & Astrophysics, The Pennsylvania State University, 525 Davey Lab, University Park, PA 16802, USA
[21] Center for Exoplanets and Habitable Worlds, The Pennsylvania State University, 525 Davey Lab, University Park, PA 16802, USA
[22] 5 Inverness Way, Hillsborough, CA 94010, USA
[23] Department of Physics and Astronomy, Swarthmore College, Swarthmore, PA 19081, USA
[24] Department of Physics, Westminster College, New Wilmington, PA 16172, USA

ABSTRACT

We report the discovery of KELT-14b and KELT-15b, two hot Jupiters from the KELT-South survey. KELT-14b, an independent discovery of the recently announced WASP-122b, is an inflated Jupiter mass planet that orbits a $\sim 5.0^{+0.3}_{-0.7}$ Gyr, $V = 11.0$, G2 star that is near the main sequence turnoff. The host star, KELT-14 (TYC 7638-981-1), has an inferred mass $M_* = 1.18^{+0.05}_{-0.07} M_\odot$ and radius $R_* = 1.37 \pm -0.08 R_\odot$, and has $T_{\rm eff} = 5802^{+95}_{-92}$ K, $\log g_* = 4.23^{+0.05}_{-0.04}$ and [Fe/H] $= 0.33 \pm -0.09$. The planet orbits with a period of 1.7100588 ± 0.0000025 days ($T_0 = 2457091.02863 \pm 0.00047$) and has a radius $R_{\rm p} = 1.52^{+0.12}_{-0.11} R_{\rm J}$ and mass $M_{\rm p} = 1.196 \pm 0.072 M_{\rm J}$, and the eccentricity is consistent with zero. KELT-15b is another inflated Jupiter mass planet that orbits a $\sim 4.6^{+0.5}_{-0.4}$ Gyr, $V = 11.2$, G0 star (TYC 8146-86-1) that is near the "blue hook" stage of evolution prior to the Hertzsprung gap, and has an inferred mass $M_* = 1.181^{+0.051}_{-0.050} M_\odot$ and radius $R_* = 1.48^{+0.09}_{-0.04} R_\odot$, and $T_{\rm eff} = 6003^{+56}_{-52}$ K, $\log g_* = 4.17^{+0.02}_{-0.04}$ and [Fe/H] $= 0.05 \pm 0.03$. The planet orbits on a period of 3.329441 ± 0.000016 days ($T_0 = 2457029.1663 \pm 0.0073$) and has a radius $R_{\rm p} = 1.443^{+0.11}_{-0.057} R_{\rm J}$ and mass $M_{\rm p} = 0.91^{+0.21}_{-0.22} M_{\rm J}$ and an eccentricity consistent with zero. KELT-14b has the second largest expected emission signal in the K-band for known transiting planets brighter than $K < 10.5$. Both KELT-14b and KELT-15b are predicted to have large enough emission signals that their secondary eclipses should be detectable using ground-based observatories.

Key words: planetary systems – stars: individual (KELT-14, KELT-15) – techniques: photometric – techniques: radial velocities – techniques: spectroscopic

Supporting material: data behind figures, machine-readable tables

1. INTRODUCTION

The confirmation of over 1000 transiting exoplanets to date is due to the success of ground-based photometric surveys such as HATNet (Bakos et al. 2004), SuperWASP (Pollacco et al. 2006), XO (McCullough et al. 2006), and TrES (Alonso et al. 2004), and the space-based missions CoRoT (Baglin et al. 2006) and *Kepler* (Borucki et al. 2010). The field has shifted from pure discovery to understanding the demographics of exoplanets and atmospheric characterization. However, many of the discovered planets are too faint or too small for performing atmospheric characterization with current facilities. To date, there are only 29 giant transiting planets orbiting stars with $V < 11.5$ in the southern hemisphere.[25]

___

[25] www.exoplanets.org, as of 2015 September.

It is believed that "hot Jupiters," gas giant planets that orbit extremely close (orbital periods of a few days) to their host stars, must form beyond the "Snow Line." Once formed, the giant planets can migrate inward through various methods (Tanaka et al. 2002; Masset & Papaloizou 2003; D'Angelo & Lubow 2008; Jackson et al. 2008; Cloutier & Lin 2013). It has been proposed that Jupiter experienced migration early in its lifetime, but did not migrate all the way inward due to the gravitational pull of Saturn (Walsh et al. 2011). These hot Jupiters, specifically ones orbiting solar-like stars, provide insight into alternate evolutionary scenarios.

The Kilodegree Extremely Little Telescope (KELT) exoplanet survey, operated and owned by Vanderbilt University, Ohio State University, and Lehigh University, has been observing >60% of the sky with a cadence of 10–20 minutes for many years. The project uses two telescopes, KELT-North at Winer Observatory in Sonoita, Arizona and KELT-South at the South African Astronomical Observatory (SAAO) in Sutherland, South Africa. The survey is optimized for high-precision ($\leqslant 1\%$ rms) photometry for stars with $8 \leqslant V \leqslant 11$ to enable transit discovery of giant planets. Each telescope has a 42 mm aperture, $26° \times 26°$ field of view, and a pixel scale of $23''/$pixel (Pepper et al. 2007, 2012). The first telescope in the survey, KELT-North, has announced six planets orbiting stars brighter than $V = 11$ (Beatty et al. 2012; Siverd et al. 2012; Pepper et al. 2013; Collins et al. 2014; Bieryla et al. 2015; Fulton et al. 2015). The younger counterpart in the survey, KELT-South, has already announced one planet, KELT-10b (Kuhn et al. 2015).

In this paper, we present the discovery of a new hot Jupiter by KELT-South, which we name KELT-15b. We also present another hot Jupiter, which we refer to in this paper as KELT-14b. Shortly before the completion of this paper, a draft manuscript was posted to the arXiv (Turner et al. 2015) describing the discovery of three new exoplanets by the SuperWASP survey. One of the planets they name WASP-122b, which is the same planet we designate as KELT-14b. Since the data we present in this paper were collected independently and the analysis performed before the announcement of WASP-122b, we have chosen to discuss our findings as an independent discovery of this planet, and we refer to it here as KELT-14b. However, we acknowledge the prior announcement of it as WASP-122b.

The paper is organized as follows with each section including both discovered systems, KELT-14b and KELT-15b. In Section 2 we present our discovery and follow-up observations (photometric and spectroscopic). We present our stellar characterization analysis and results in Section 3. The global modeling and resulting planetary parameters are discussed in Section 4 with our false positive analysis described in Section 5. In Section 6 we describe the evolutionary analysis, long-term follow-up to look for additional companions in each system, and the value each planetary system has for future atmospheric characterization observations. We summarize our results and conclusions in Section 7.

2. DISCOVERY AND FOLLOW-UP OBSERVATIONS

2.1. KELT-South

KELT-14 and KELT-15 are located in the KELT-South field 34, which is centered at J2000 $\alpha = 08^h16^m12^s \delta = -54°00'00''$. Field 34 was monitored in two separate campaigns:

first from UT 2010 January 03 to UT 2010 February 19 as part of the KELT-South commissioning campaign, and then again from UT 2012 September 16 to UT 2014 June 14, acquiring a total of ~5780 images after post-processing and removal of bad images. Following the strategy described in Kuhn et al. (2015), we reduced the raw images, extracted the light curves, and searched for transit candidates. Two stars emerged as top candidates from this process: KS34C030815 (TYC 7638-981-1, GSC 07638-00981, 2MASS J07131235-4224350) located at $\alpha = 07^h13^m12^s347$ $\delta = -42°24'35''17$ J2000, hereafter as KELT-14, and KS34C034621 (TYC 8146-86-1, GSC 08146-00086, 2MASS J07493960-5207136) located at $\alpha = 07^h49^m39^s606 \delta = -52°07'13''58$ J2000, designated as KELT-15 (see Figure 1). The host star properties for both targets are listed in Table 1. We used the box-fitting least squares (BLS) algorithm (Kovács et al. 2002; Hartman 2012) to select these candidates, and the BLS selection criteria and values for both are shown in Table 2.

2.2. Photometric Follow-up

To precisely measure the transits of KELT-14b and KELT-15b, we obtained high-cadence, high-precision photometric follow-up using larger telescopes that cleanly resolve the hosts from their neighbors within a few arcseconds. These observations better constrain the period, depth, and duration of the transit and also rule out various false positive scenarios. To predict the transits, we use the web interface, TAPIR (Jensen 2013). For consistency, all follow-up observations were analyzed using AstroImageJ (AIJ) (Collins & Kielkopf 2013; Collins 2015). This software also provides the best detrending parameters that are included in the global fit (see Section 4.1). The follow-up photometry for KELT-14b and KELT-15b are shown in Figures 2 and 3 respectively. (See Table 3 for a list of the photometric follow-up observations.)

2.2.1. LCOGT

We observed a nearly full transit of KELT-14b in the Sloan g-band on UT 2015 March 29 from a 1 m telescope in the Las Cumbres Observatory Global Telescope (LCOGT) network[26] located at Cerro Tololo Inter-American Observatory (CTIO) in Chile. The LCOGT telescopes at CTIO have a $4 K \times 4 K$ Sinistro detector with a $27' \times 27'$ field of view and a pixel scale of $0.''39$ per pixel. The typical FWHM of the star in this data set was 11.24 pixels. The reduced data were downloaded from the LCOGT archive and analyzed using the AIJ software. In a portion of the light curve surrounding the transit ingress the target was saturated, therefore we exclude this portion of the data from the global parameter analysis in Section 4.1.

2.2.2. PEST Observatory

PEST (Perth Exoplanet Survey Telescope) observatory is a home observatory owned and operated by Thiam-Guan (TG) Tan. It is equipped with a 12 inch Meade LX200 SCT $f/10$ telescope with focal reducer yielding $f/5$. The camera is an SBIG ST-8XME with a filter wheel having B, V, R, I and Clear filters. The focusing is computer controlled with an Optec TCF-Si focuser. The image scale obtained is $1.''2$ per pixel and a full frame image covers $31' \times 21'$. For images in focus the usual star FWHM achieved is about 2.5–3.5 pixels. The PEST
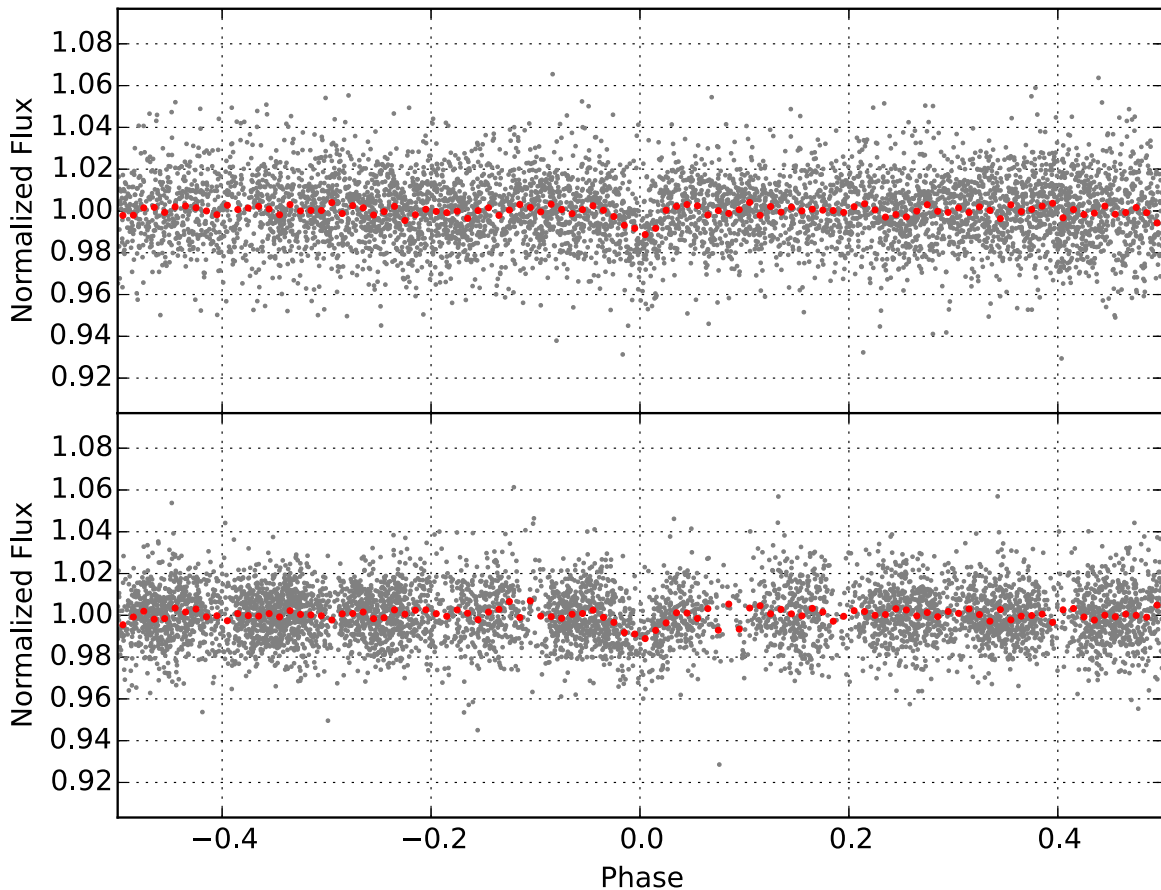
---

[26] http://lcogt.net/

Figure 1. Discovery light curve of KELT-14b (top) and KELT-15b (bottom) from the KELT-South telescope. The light curves are phase-folded to the discovery periods of $P = 1.7100596$ and 3.329442 days respectively; the red points show the light curve binned in phase using a bin size of 0.01.

observatory clock is synced on start up to the atomic clock in Bolder, CO and is resynced every 3 hr. PEST observed full transits of KELT-14b on UT 2015 January 20 (*R*) and UT 2015 January 25 (*I*), and a nearly full transit on UT 2015 March 09 (*V*). PEST observed a full transit of KELT-15b on UT 2015 January 16 (*I*).

2.2.3. Hazelwood Observatory

The Hazelwood Observatory is a backyard observatory with 0.32 m Planewave CDK telescope working at *f*/8, a SBIG ST8XME 1.5 K × 1 K CCD, giving a 18′ × 12′ field of view and 0″.73 per pixel. The camera is equipped with Clear, *B*, *V*, *Rc*, and *Ic* filters (Astrodon Interference). Typical FWHM is 2″.4–2″.7. The Hazelwood Observatory, operated by Chris Stockdale in Victoria, Australia, obtained an ingress of KELT-14b in *V*-band on UT 2015 March 09, a full transit in the *B*-band on UT 2015 March 21 and a full transit in *I*-band on UT 2015 April 02. The observatory computer clock is synchronised at the start of each observing session and then every 15 minutes using NTP protocol to time.nist.gov. ACP, ACP Scheduler and MaximDL are used to acquire the images. The camera shutter latency (0.5 s) is allowed for within MaximDL and the adjusted exposure time is recorded within the FITS header. Experience with another project has shown that the exposure start time is recorded in the FITS header to within one second of the actual exposure start time.

2.2.4. Adelaide Observations

The Adelaide Observatory, owned and operated by Ivan Curtis is located in Adelaide, Australia (labeled "ICO" in the figures). The observatory is equipped with a 9.25-in Celestron SCT telescope with an Antares 0.63x focal reducer yielding an overall focal ratio of *f*/6.3. The camera is an Atik 320e, which uses a cooled Sony ICX274 CCD of 1620 × 1220 pixels. The field of view is 16′.6 × 12′.3 with a pixel scale of 0″.62 per pixel and a typical FWHM around 2″.5–3″.1. The observatory's computer clock is synced with an internet time server before each observation session and has an overall timing uncertainty of a few seconds. The Adelaide Observatory observed a full transit of KELT-14b on UT 2015 March 09 (*V*) and full transits of KELT-15b on UT 2014 December 27 (*R*) and UT 2015 January 06 (*R*).

2.3. Spectroscopic Follow-up

2.3.1. Reconnaissance Spectroscopy

Since many astrophysical phenomena can create photometric signals that mimic planetary transits, it is important to follow up all candidates carefully to eliminate false positives. After identifying the targets as planet candidates from the KELT photometry, a first stage of spectroscopic reconnaissance was done using the WiFeS spectrograph mounted on the 2.3 m ANU telescope at Siding Spring Observatory (Dopita et al. 2007). This instrument is an optical dual-beam, image-slicing integral-field spectrograph. The full WiFeS observing

Table 1
Stellar Properties of KELT-14 and KELT-15 Obtained from the Literature

Parameter	Description	KELT-14 Value	KELT-15 Value	Source	Reference(s)
		TYC 7638-981-1	TYC 8146-86-1		
		GSC 07638-00981	GSC 08146-00086		
		2MASS J07131235-4224350	2MASS J07493960-5207136		
α_{J2000}	Right Ascension (R.A.)	07:13:12.347	07:49:39.606	Tycho-2	Høg et al. (2000)
δ_{J2000}	Declination (Decl.)	−42:24:35.17	−52:07:13.58	Tycho-2	Høg et al. (2000)
NUV	…	17.06 ± 0.1	N/A	*GALEX*	…
B_T	Tycho B_T magnitude	11.963	11.889	Tycho-2	Høg et al. (2000)
V_T	Tycho V_T magnitude	11.088	11.440	Tycho-2	Høg et al. (2000)
Johnson V	APASS magnitude	10.948 ± 0.05	11.189 ± 0.05	APASS	Henden et al. (2015)
Johnson B	APASS magnitude	11.64 ± 0.05	11.745 ± 0.05	APASS	Henden et al. (2015)
Sloan g'	APASS magnitude	11.247 ± 0.051	11.438 ± 0.03	APASS	Henden et al. (2015)
Sloan r'	APASS magnitude	10.733 ± 0.053	11.048 ± 0.03	APASS	Henden et al. (2015)
Sloan i'	APASS magnitude	10.631 ± 0.05	10.935 ± 0.05	APASS	Henden et al. (2015)
J	2MASS magnitude	9.808 ± 0.024	10.205 ± 0.024	2MASS	Cutri et al. (2003)
H	2MASS magnitude	9.487 ± 0.024	9.919 ± 0.023	2MASS	Cutri et al. (2003)
K	2MASS magnitude	9.424 ± 0.023	9.854 ± 0.025	2MASS	Cutri et al. (2003)
WISE1	*WISE* passband	9.369 ± 0.023	9.775 ± 0.023	*WISE*	Cutri et al. (2012)
WISE2	*WISE* passband	9.414 ± 0.021	9.805 ± 0.020	*WISE*	Cutri et al. (2012)
WISE3	*WISE* passband	9.339 ± 0.026	9.919 ± 0.048	*WISE*	Cutri et al. (2012)
WISE4	*WISE* passband	9.442 ± 0.495	**<9.580**	*WISE*	Cutri et al. (2012)
μ_α	Proper Motion in R.A. (mas yr^{-1})	−13.9 ± 2.2	−3.4 ± 2.3	NOMAD	Zacharias et al. (2004)
μ_δ	Proper Motion in Decl. (mas yr^{-1})	−1.3 ± 2.0	−2.0 ± 2.9	NOMAD	Zacharias et al. (2004)
U[a]	Space motion (km s^{-1})	−4.6 ± 1.9	7.8 ± 3.8	…	This work
V	Space motion (km s^{-1})	−14.6 ± 0.9	2.6 ± 0.8	…	This work
W	Space motion (km s^{-1})	−14.0 ± 2.3	−1.5 ± 3.3	…	This work
Distance	Estimated Distance (pc)	201 ± 19	291 ± 30	…	This work
RV	Absolute RV (km s^{-1})	34.62 ± 0.13	12.20 ± 0.11	…	This work
$v \sin i_*$	Stellar Rotational Velocity (km s^{-1})	7.7 ± 0.4	7.6 ± 0.4	…	This work

Note. Bold value corresponds to upper limits (S/N < 2).
[a] U is positive in the direction of the Galactic Center.

Table 2
KELT-South BLS Selection Criteria

BLS Statistic	Selection Criteria	KELT-14b KS34C030815	KELT-15b KS34C034621
Signal detection efficiency	SDE > 7.0	7.75403	11.04677
Signal to pink-noise	SPN > 7.0	8.26194	9.78164
Transit depth	$\delta < 0.05$	0.01072	0.00841
χ^2 ratio	$\frac{\Delta\chi^2_-}{\Delta\chi^2_+} > 1.5$	2.16	2.56
Duty cycle	$q < 0.1$	0.03333	0.04667

strategy and reduction procedure is described in Bayliss et al. (2013).

First, observations of both stars were performed at low resolution ($R \sim 3000$) in the 3500–6000 Å range to determine their stellar type. Both KELT-14 and KELT-15 were identified with the following parameters: KELT-14 has $T_{eff} = 5572 \pm 200$ K, $\log g_* = 3.5 \pm 0.4$ (cgs) and [Fe/H] = 0.0 ± 0.4; KELT-15b has $T_{eff} = 6221 \pm 200$ K, $\log g_* = 3.4 \pm 0.4$ (cgs) and [Fe/H] = 0.0 ± 0.4. The low resolution spectra provide poor precision on the $\log g_*$ and therefore, these $\log g_*$ values are not very reliable.

Additionally, three observations for each target were performed in medium-resolution ($R \sim 7000$) using the red camera arm of the WiFeS spectrograph (5500–9000 Å) across the expected orbital phase based on the photometrically detected period. These observations were aimed at performing multiple radial velocity (RV) measurements of each target to detect signals higher than 5 km s^{-1} amplitude, allowing us to identify grazing binary systems or blended eclipsing binaries. The typical RV precision achieved with this instrument is around 1.5 km s^{-1}, and both targets showed no significant variations among the three measurements.

2.3.2. High Precision Spectroscopic Follow-up

To confirm the planetary nature of the companion, we obtain multi-epoch high-resolution spectroscopy. These spectra allow us to very accurately measure the RV of the host star providing us with a precise measurement of the companion's mass. Also, these spectra provide a much better estimate of the stellar properties.
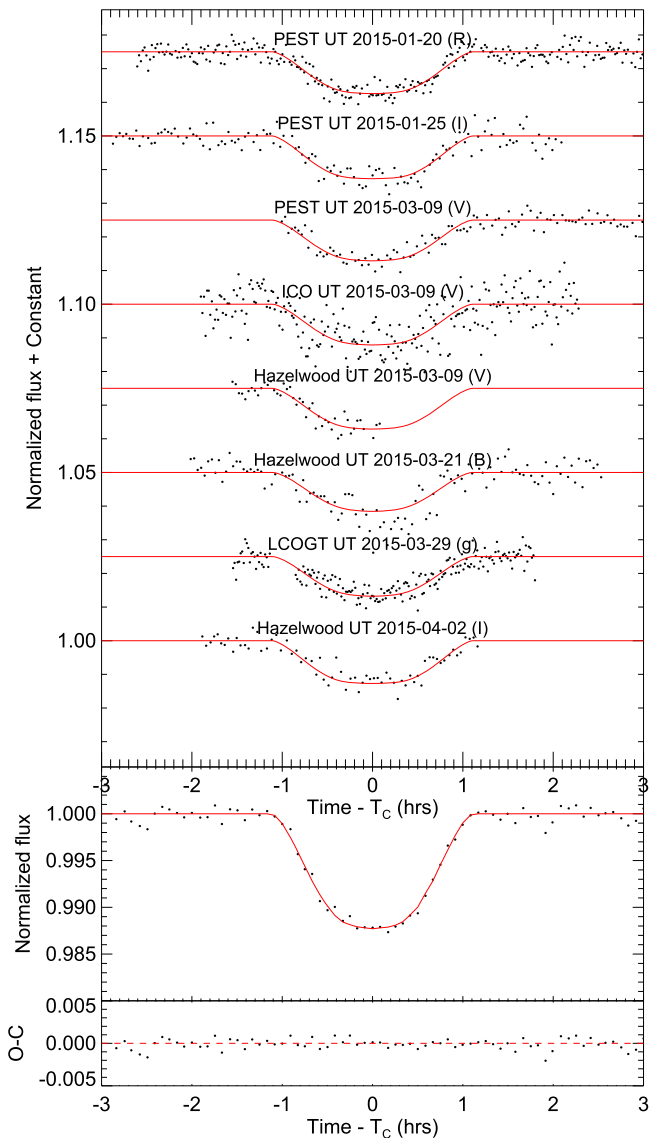
Figure 2. (Top) The follow-up photometry of KELT-14b from the KELT follow-up network. The red line is the best model for each follow-up lightcurve. (Bottom) The individual follow-up lightcurves combined and binned in 5 minute intervals. This combined and binned plot represents the true nature of the transit. The combined and binned light curve is for display and is not used in the analysis. The red line represents the combined and binned individual models (red) of each follow-up observation.

(The data used to create this figure are available.)
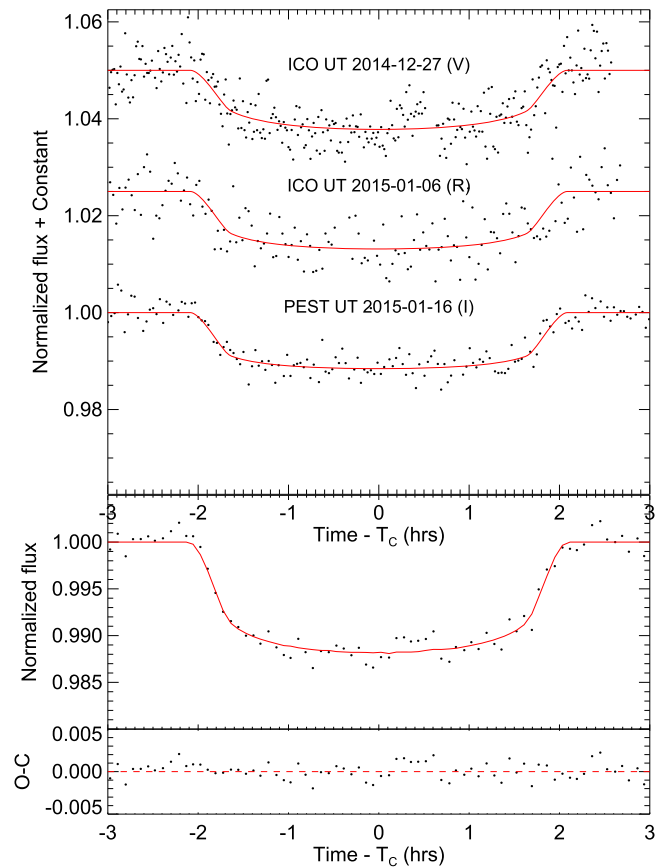

Figure 3. (Top) The follow-up photometry of KELT-15b from the KELT follow-up network. The red line is the best model for each follow-up lightcurve. (Bottom) All the follow-up lightcurves combined and binned in 5 minute intervals. This best represents the true nature of the transit. The combined and binned light curve is for display and is not used in the analysis. The red line represents the combined and binned individual models (red) of each follow-up observation.

(The data used to create this figure are available.)

2.3.3. CYCLOPS2

Spectroscopic observations of KELT-14 and KELT-15 were carried out using the CYCLOPS2 fiber feed with the UCLES spectrograph instrument on the Anglo-Australian Telescope (AAT) over two observing runs: UT 2015 February 02—UT 2015 March 01 and UT 2015 May 6—UT 2015 May 13 (see Figures 4 and 5). The instrumental set-up and observing strategy for these observations closely follow that described in earlier CYCLOPS RV papers (Addison et al. 2013, 2014).

CYCLOPS2 is a Cassegrain fiber-based integral field unit which reformats a $\sim 2\rlap{.}{''}5$ diameter on-sky aperture into a pseudo-slit of dimensions equivalent to $0\rlap{.}{''}6$ wide $\times 14\rlap{.}{''}5$ long (Horton et al. 2012). CYCLOPS2 has 16 on-sky fibers, plus

one fiber illuminated by a ThUXe lamp. Each fiber delivers a spectral resolution of $\lambda/\Delta\lambda \approx 70{,}000$ over 19 echelle orders in the wavelength range of 4550–7350 Å, when used with the UCLES spectrograph in its 79 line/mm grating configuration.

We use a ThAr calibration lamp to illuminate all of the on-sky fibers at the beginning of observations to create a *reference* ThAr wavelength solution. We then use simultaneous ThUXe data from each exposure to determine low-order distortions which differentially calibrate observations through the night onto the *reference* ThAr solution. These reductions are carried out using custom MATLAB routines (D. Wright & C. G. Tinney 2016, in preparation). Calibration precision is estimated from the scatter of fits to the simultaneous ThUXe spectral features and these are tested against velocity standards taken each night. The typical calibration precision is $<10\,\mathrm{m\,s^{-1}}$. This calibration error is combined with the error from a fit to the cross-correlation profile to give a final uncertainty for each observation.

The cross-correlation profiles are obtained using a weighted cross-correlation (Baranne et al. 1996; Pepe et al. 2002) of a stellar template produced with SYNSPEC (Hubeny & Lanz 2011). The velocities are determined from the fit of a generalised normal distribution to the cross-correlation profiles and the

Target	Observatory	Date (UT)	Filter	FOV	Pixel Scale	Exposure (s)	FWHM	Detrending Parameters for Global Fit
KELT-14b	PEST	UT 2015 Jan 20	R	$31' \times 21'$	$1\rlap{.}''2$	60	6.04	airmass, y coordinates
KELT-14b	PEST	UT 2015 Jan 25	I	$31' \times 21'$	$1\rlap{.}''2$	120	7.48	airmass, y coordinates
KELT-14b	PEST	UT 2015 Mar 09	V	$31' \times 21'$	$1\rlap{.}''2$	120	5.56	airmass
KELT-14b	Adelaide	UT 2015 Mar 09	V	$16\rlap{.}'6 \times 12\rlap{.}'3$	$0\rlap{.}''62$	60	10.48	airmass, total counts
KELT-14b	Hazelwood	UT 2015 Mar 09	V	$18' \times 12'$	$0\rlap{.}''73$	120	6.10	airmass
KELT-14b	Hazelwood	UT 2015 Mar 21	B	$18' \times 12'$	$0\rlap{.}''73$	120	6.31	airmass
KELT-14b	LCOGT	UT 2015 Mar 29	g'	$27' \times 27'$	$0\rlap{.}''39$	39	11.24	airmass, pixel width, total counts
KELT-14b	Hazelwood	UT 2015 Apr 02	I	$18' \times 12'$	$0\rlap{.}''73$	120	7.19	airmass
KELT-15b	Adelaide	UT 2014 Dec 27	V	$16\rlap{.}'6 \times 12\rlap{.}'3$	$0\rlap{.}''62$	60	9.95	airmass, y coordinates, total counts
KELT-15b	Adelaide	UT 2015 Jan 06	R	$16\rlap{.}'6 \times 12\rlap{.}'3$	$0\rlap{.}''62$	120	13.8	airmass, y coordinates
KELT-15b	PEST	UT 2015 Jan 16	I	$31' \times 21'$	$1\rlap{.}''2$	120	6.35	airmass, sky counts per pixel, total counts

errors are estimated from the Jacobian matrix for each fit. We find no correlation between the bisector spans and the measured radial velocities. This provides strong evidence against a blended eclipsing binary scenario.

2.3.4. CORALIE

CORALIE is a fiber-fed echelle spectrograph (Queloz et al. 2001) attached to the Swiss 1.2 m Leonard Euler telescope at the ESO La Silla Observatory in Chile. It has a spectral resolution of $R \sim 60{,}000$, a wavelength range of 3900–6800 Å, and is able to measure radial velocities of bright stars to a precision of $3\,\mathrm{m\,s^{-1}}$ or better (Pepe et al. 2002). In 2015 June, the CORALIE spectrograph was equipped with a new Fabry–Pérot-based calibration system (Wildi et al. 2011). This system replaces the ThAr lamp for the simultaneous reference method that determines and corrects for instrumental drift occurring between the calibration and the science exposure (Baranne et al. 1996). The data-reduction software has been adapted to take into account the new operational mode and take benefit from the higher spectral content, and hence the lower photon noise, on the drift measurement, provided by the Fabry–Pérot based calibration source. We obtained spectra at five epochs of KELT-15 from UT 2015 September 02 to UT 2015 September 14. All observations were reduced and radial velocities were computed in real time using the standard CORALIE pipeline. The observations from CORALIE are consistent with the CYCLOPS2 measured radial velocities. The results are shown in Figure 5. We find no correlation between the bisector spans and the measured radial velocities (see Figure 6).

3. ANALYSIS AND RESULTS

3.1. SME Stellar Analysis

In order to determine precise stellar parameters for KELT-14 and KELT-15, we use the available high-resolution, low signal-to-noise ratio (S/N) AAT CYCLOPS2 spectra acquired for RV confirmation of the two planetary systems. For each CYCLOPS2 dataset, we took the flux weighted mean of the individual fibers, continuum normalized each spectral order, and stitched the orders into a single 1D spectrum. We shifted each resulting spectrum to rest wavelength by accounting for barycentric motion, and median combined all observations into a single spectrum with a S/N ~ 50, sufficient for detailed spectroscopic analysis.

Stellar parameters for KELT-14 and KELT-15 are determined using an implementation of Spectroscopy Made Easy (SME) (Valenti & Piskunov 1996). Our Monte Carlo approach to using SME for measuring stellar parameters is detailed in Kuhn et al. (2015). Briefly, we use a multi-trial minimization of 500 randomly selected initial parameter values, each solving for five free parameters: effective temperature (T_{eff}), surface gravity ($\log g_*$), iron abundance ([Fe/H]), metal abundance ([m/H]), and rotational velocity of the star ($v \sin i_*$). We determine our final measured stellar properties by identifying the output parameters that give the optimal SME solution (i.e., the solution with the lowest χ^2). The overall SME measurement uncertainties in the final parameters are calculated by adding in quadrature the internal error determined from the 68.3% confidence region in the χ^2 map, the median absolute deviation of the parameters from the 500 output SME solutions to account for the correlation between the initial guess and the final fit, and an estimate for the systematic errors in our method when compared to other common stellar spectral analysis tools (see Gómez Maqueo Chew et al. 2013).

Due to the instrument setup used for measuring high-precision radial velocities, the AAT CYCLOPS2 spectra do not include the full MgB triplet wavelength region, a pressure-broadened set of lines commonly used in spectral synthesis modeling to constrain $\log g_*$ (Valenti & Fischer 2005). The available spectra only include one of the three strong Mg lines in this region. In order to investigate the effect of this constraint on our stellar parameters, we run two separate SME runs for both KELT-14 and KELT-15, one with $\log g_*$ as a free parameter and the other with $\log g_*$ fixed from our preliminary global fit of the photometric observations.

Our final SME spectroscopic parameters for KELT-14 are: $T_{\mathrm{eff}} = 5817 \pm 90$ K, $\log g_* = 4.16 \pm 0.12$, [m/H] $= 0.39 \pm 0.03$, [Fe/H] $= 0.34 \pm 0.09$ and a projected rotational velocity $v \sin i_* = 7.7 \pm 0.4\,\mathrm{km\,s^{-1}}$. Similarly, with a fixed $\log g_* = 4.23$; $T_{\mathrm{eff}} = 5834 \pm 75$ K, [m/H] $= 0.39 \pm 0.03$, [Fe/H] $= 0.34 \pm 0.09$ and $v \sin i_* = 7.6 \pm 0.4\,\mathrm{km\,s^{-1}}$. For KELT-15 we find: $T_{\mathrm{eff}} = 6023 \pm 61$ K, $\log g_* = 3.80 \pm 0.08$, [m/H] $= 0.06 \pm 0.03$, [Fe/H] $= 0.05 \pm 0.03$ and $v \sin i_* = 11.1 \pm 0.5\,\mathrm{km\,s^{-1}}$. With a fixed $\log g_* = 4.17$ we find; $T_{\mathrm{eff}} = 6102 \pm 51$ K, [m/H] $= 0.02 \pm 0.03$, [Fe/H] $= 0.05 \pm 0.03$ and $v \sin i_* = 11.1 \pm 0.5\,\mathrm{km\,s^{-1}}$. We constrain the macro- and microturbulent velocities to the empirically constrained relationship (Gómez Maqueo Chew et al. 2013). However, we do allow them to change during our modeling according to the other stellar parameters. Our best fitting stellar parameters

Table 4
Spectroscopic Follow-up Observations

| Target	Telescope/Instrument	Date Range	Type of Observation	Resolution	Wavelength Range	Mean S/N	Epochs
KELT-14	ANU 2.3/WiFes	UT 2015 Feb 02	Reconnaissance	$R \sim 3000$	3500–6000 Å	75	1
KELT-14	ANU 2.3/WiFes	UT 2015 Feb 02–UT 2015 Feb 04	Reconnaissance	$R \sim 7000$	5200–7000 Å	85	3
KELT-15	ANU 2.3/WiFes	UT 2014 Dec 29	Reconnaissance	$R \sim 3000$	3500–6000 Å	110	1
KELT-15	ANU 2.3/WiFes	UT 2014 Dec 29–UT 2015 Jan 02	Reconnaissance	$R \sim 7000$	5200–7000 Å	80	3
KELT-14	AAT/CYCLOPS2	UT 2015 Feb 26–UT 2015 May 13	High Resolution	$R \sim 70,000$	4550–7350 Å	41.6	15
KELT-15	AAT/CYCLOPS2	UT 2015 Feb 27–UT 2015 May 15	High Resolution	$R \sim 70,000$	4550–7350 Å	41.2	14
KELT-15	Euler/CORALIE	UT 2015 Sep 04–UT 2015 Sep 13	High Resolution	$R \sim 60,000$	3900–6800 Å	28.25	5
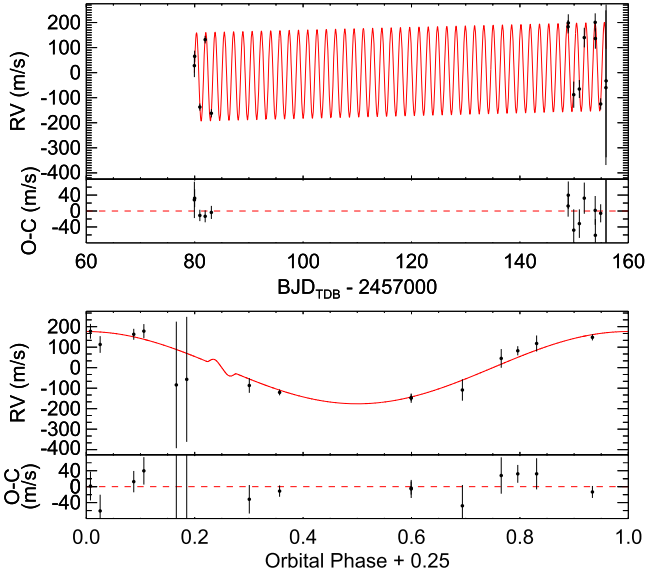
Figure 4. (Top) The AAT radial velocity measurements (the median absolute RV has been subtracted off) and residuals for KELT-14. The best-fitting orbit model is shown in red. The residuals of the RV measurements to the best fitting model are shown below. (Bottom) The KELT-14 AAT measurements phase-folded to the final global fit ephemeris.
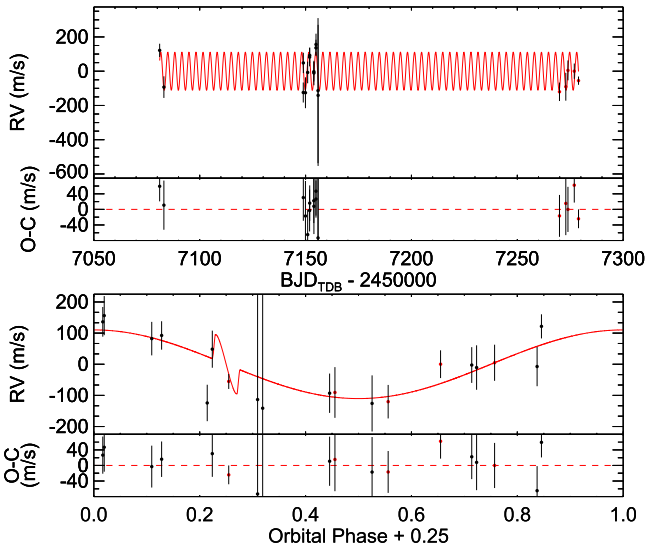

Figure 5. (Top) The AAT (black) and CORALIE (red) radial velocity measurements (the median absolute RV has been subtracted off) and residuals for KELT-15. The best-fitting orbit model is shown in red. The residuals of the RV measurements to the best model are shown below. (Bottom) The KELT-15 AAT (black) and CORALIE (red) measurements phase-folded to the final global fit ephemeris.

result in $v_{\mathrm{mac}} = 4.05\,\mathrm{km\,s^{-1}}$ and $v_{\mathrm{mic}} = 1.00\,\mathrm{km\,s^{-1}}$ for KELT-14, and for KELT-15 $v_{\mathrm{mac}} = 4.37\,\mathrm{km\,s^{-1}}$ and $v_{\mathrm{mic}} = 1.19\,\mathrm{km\,s^{-1}}$.

3.2. Spectral Energy Distribution (SED) Analysis

We construct empirical SEDs of KELT-14 and KELT-15 using all available broadband photometry in the literature, shown in Figure 7. We use the near-UV flux from *GALEX* (Martin et al. 2005), the B_T and V_T fluxes from the Tycho-2 catalog, B, V, g', r', and i' fluxes from the AAVSO APASS catalog, NIR fluxes in the J, H, and K_S bands from the 2MASS
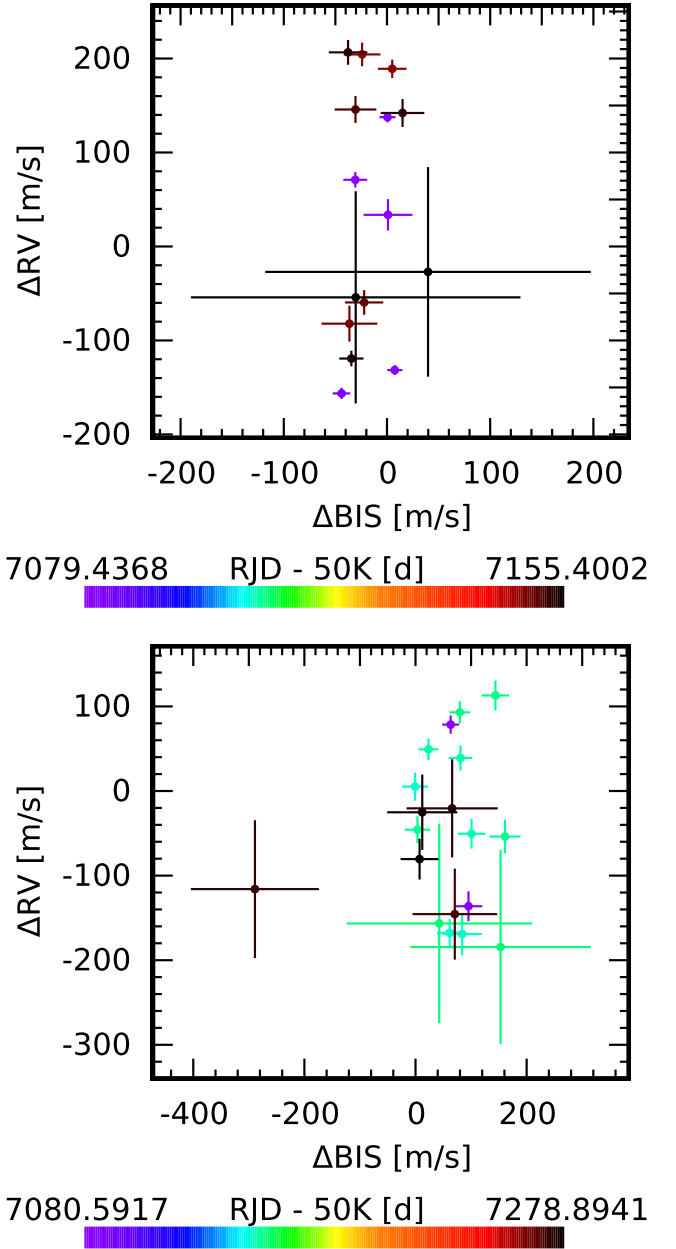

Figure 6. The AAT Bisector measurements for the (top) KELT-14 and the combined AAT and CORALIE bisector measurements for (bottom) the KELT-15 spectra used for radial velocity measurements. We find no significant correlation between RV and the bisector spans.

Point Source Catalog (Cutri et al. 2003; Skrutskie et al. 2006), and near- and mid-infrared fluxes in the *WISE* passbands (Wright et al. 2010).

We fit these fluxes using the Kurucz atmosphere models (Castelli & Kurucz 2004) by fixing the values of T_{eff}, $\log g_*$ and [Fe/H] inferred from the global fit to the lightcurve and RV data as described in Section 4.1 and listed in Tables 5 and 6, and then finding the values of the visual extinction A_V and distance d that minimize χ^2, with a maximum permitted A_V based on the full line of sight extinction from the dust maps of Schlegel et al. (1998) (maximum $A_V = 0.50$ mag and 0.89 mag for KELT-14 and KELT-15, respectively). Note that while the final best SED fits below are in fact well fit with $A_V \equiv 0$, we
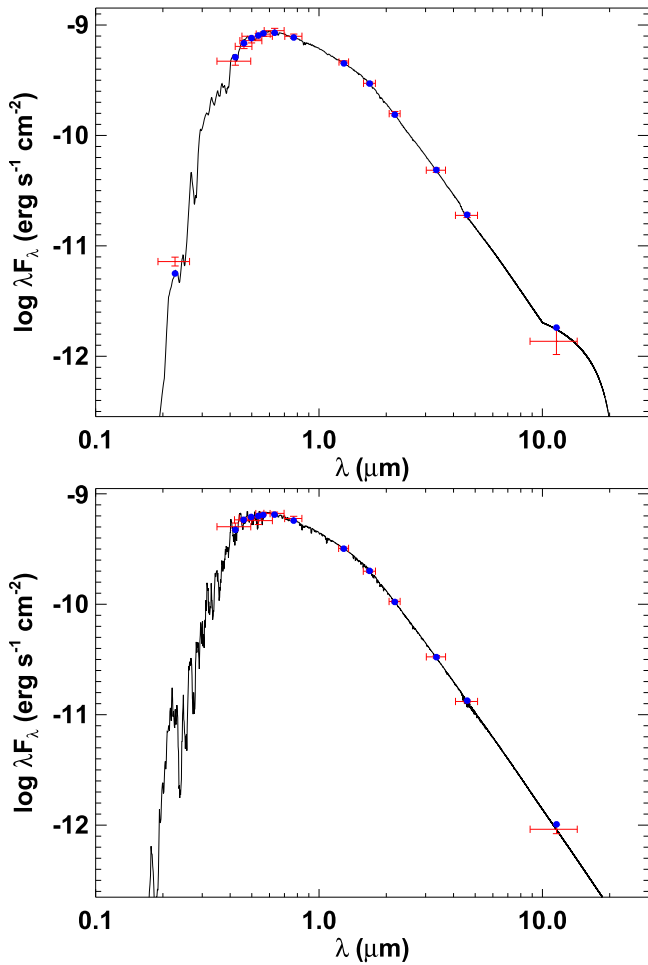
Figure 7. The SED fit for (top) KELT-14 and (bottom) KELT-15. The red points show the photometric values and errors given in Table 1. The blue points are the predicted integrated fluxes at the corresponding bandpass. The black line represents the best fit stellar atmospheric model.

Table 5
KELT-14 Radial Velocity Observations with CYCLOPS2

BJD_{TDB}	RV (m s^{-1})	RV Error (m s^{-1})	Instrument
2457079.939623842	34621.30	16.70	CYCLOPS2
2457079.991772522	34658.60	8.20	CYCLOPS2
2457080.950428010	34456.10	5.20	CYCLOPS2
2457081.937382183	34725.20	5.50	CYCLOPS2
2457083.075531623	34431.30	6.00	CYCLOPS2
2457148.892669835	34776.70	9.80	CYCLOPS2
2457148.924568460	34792.00	12.60	CYCLOPS2
2457149.929456027	34505.50	19.10	CYCLOPS2
2457150.967262368	34528.10	13.10	CYCLOPS2
2457151.873724511	34733.40	14.30	CYCLOPS2
2457153.886260897	34794.20	13.20	CYCLOPS2
2457153.916879608	34729.70	14.90	CYCLOPS2
2457154.898109197	34468.40	8.30	CYCLOPS2
2457155.867229521	34533.50	112.90	CYCLOPS2
2457155.900058155	34560.60	111.50	CYCLOPS2

(This table is available in machine-readable form.)

Table 6
KELT-15 Radial Velocity Observations with CYCLOPS2 and CORALIE

BJD_{TDB}	RV (m s^{-1})	RV error (m s^{-1})	Instrument
2457081.094367965	12320.4	10.8	CYCLOPS2
2457083.091453823	12105.7	17.6	CYCLOPS2
2457148.910598987	12074.4	16.3	CYCLOPS2
2457148.942507928	12247.1	16.6	CYCLOPS2
2457149.947425124	12072.9	25.1	CYCLOPS2
2457150.985251112	12191.4	17.6	CYCLOPS2
2457151.891071429	12281.0	15.0	CYCLOPS2
2457151.953179348	12291.2	12.7	CYCLOPS2
2457153.903635089	12196.2	16.0	CYCLOPS2
2457153.934254059	12188.1	19.9	CYCLOPS2
2457154.912681718	12334.9	13.3	CYCLOPS2
2457154.921681414	12354.9	17.5	CYCLOPS2
2457155.886209486	12085.3	118.0	CYCLOPS2
2457155.918108410	12057.5	114.8	CYCLOPS2
2457269.908610	12096.39	53.81	CORALIE
2457272.903199	12125.96	81.47	CORALIE
2457273.907330	12221.40	57.97	CORALIE
2457276.897042	12216.76	44.60	CORALIE
2457278.894140	12161.43	24.16	CORALIE

(This table is available in machine-readable form.)

did include A_V as a free fit parameter because of the a priori likelihood of A_V as large as 0.50–0.89 mag.

For KELT-14 we find $A_V = 0.1 \pm 0.1$ mag and $d = 201 \pm 19$ pc with the best fit model having a reduced $\chi^2 = 1.39$. For KELT-15 we find $A_V = 0.18 \pm 0.12$ and $d = 291 \pm 30$ pc with the best fit model having a reduced $\chi^2 = 0.84$. This implies a very good quality of fit and further corroborates the final derived stellar parameters for the KELT-14 and KELT-15 host stars. We note that the quoted statistical uncertainties on A_V and d are likely to be underestimated because alternate model atmospheres would predict somewhat different SEDs and thus values of extinction and distance, but for stars of the masses and temperatures of KELT-14 and KELT-15 the systematic differences among various model atmospheres are not expected to be large.

3.3. Evolutionary State

To better place the KELT-14 and KELT-15 systems in context, we show in Figure 8 the H–R diagrams for the two systems in the T_{eff} versus $\log g_*$ plane. In each case, we use the Yonsei-Yale (YY) stellar evolution model track (Demarque et al. 2004) for a star with the mass and metallicity inferred from the final global fit. Specifically, we are using the global fit where the SME determined [Fe/H] and T_{eff}, where $\log g_*$ was not fixed, as priors (see Section 4.1). The shaded region represents the mass and [Fe/H] fit uncertainties. The model isochrone ages are indicated as blue points, and the final best global fit T_{eff} and $\log g_*$ values are represented by the red error bars. For comparison, the T_{eff} and $\log g_*$ values determined from spectroscopy alone (without fixing $\log g_*$) are represented by the green error bars, while the blue error bars represent the case with $\log g_*$ fixed in the SME analysis (Figure 8).

KELT-14 is a G2 type star near the main-sequence turnoff but not yet in the Hertzsprung gap, with an age of $\sim 5.0^{+0.3}_{-0.7}$ Gyr. KELT-15 is a G0 type star with an age of $\sim 4.6^{+0.5}_{-0.4}$ Gyr, on or near the "blue hook" just prior to the
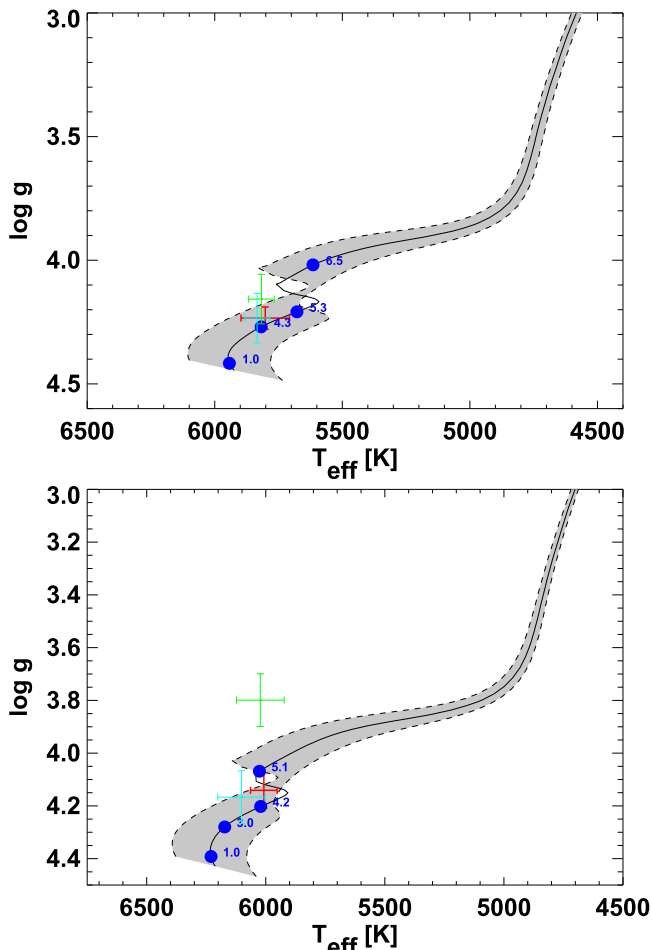
Figure 8. The theoretical H–R diagrams for (top) KELT-14 and (bottom) KELT-15 using the Yonsei-Yale stellar evolution models (Demarque et al. 2004). The $\log g_\star$ values are in cgs units. The red cross represents the values from the final global fit. The blue cross is the position and errors of the SME analysis when $\log g_\star$ was fixed at the initial global fit value and the green cross is when $\log g_\star$ was not fixed. The dashed lines at the edge of the gray shaded region represent the 1σ uncertainties on $M_\star$ and [Fe/H] from the global fit. The various ages along the tracks are represented by the blue points.

Hertzsprung gap. These classifications are also consistent with those reported in the catalogs of Pickles & Depagne (2010) and Ammons et al. (2006). Note that the observed rotational velocities of the stars (7–11 km s^{-1}; see Section 3.1) are consistent with the 2–15 km s^{-1} range observed for solar-type stars with the masses and ages of KELT-14 and KELT-15 (e.g., Soderblom 1983).

3.4. UVW Space Motion

To better understand the place of KELT-14 and KELT-15 in the galaxy, we calculate the UVW space motion. This exercise can allow us to determine the membership and possibly the age of a star if it is associated with any known stellar groups. To calculate the UVW space motion, we combine the information presented in Table 1 with the determined distance to KELT-14 and KELT-15 from the SED analysis (201 ± 19 pc and 291 ± 30 pc respectively). We also estimated the absolute RV and error by taking the average and standard deviation of all the measured radial velocities by AAT. This gave us an estimated absolute RV of 34.62 ± 0.13 km s^{-1} and 12.20 ± 0.11 m s^{-1} for KELT-14b and KELT-15b, respectively. We calculate the

space motion to be $U = -4.6 \pm 1.9$ km s^{-1}, $V = -14.6 \pm 0.9$ km s^{-1}, $W = -14.0 \pm 2.3$ km s^{-1} for KELT-14 and $U = 7.8 \pm 3.8$ km s^{-1}, $V = 2.6 \pm 0.8$ km s^{-1}, $W = -1.5 \pm 3.3$ km s^{-1} for KELT-15 (positive U pointing toward the Galactic center). Using the peculiar velocity of the Sun with respect local standard rest ($U = 8.5$ km s^{-1}, $V = 13.38$ km s^{-1}, and $W = 6.49$ km s^{-1}), we have corrected for this motion in our calculations of the UVW space motion of KELT-14 and KELT-15 (Coşkunoğlu et al. 2011). These space motion values give a 99% chance that both KELT-14 and KELT-15 belong to the thin disk, according to the classification scheme of Bensby et al. (2003).

4. PLANETARY PROPERTIES

4.1. EXOFAST Global Fit

To perform a global fit of our photometric and spectroscopic data, we use a modified version of the IDL exoplanet fitting tool, EXOFAST (Eastman et al. 2013). More detailed explanation of the global modeling is provided in Siverd et al. (2012). To determine a system's final parameters, simultaneous Markov Chain Monte Carlo (MCMC) analysis is performed on the AAT RV measurements and the follow-up photometric observations. To constrain $M_\star$ and $R_\star$ EXOFAST uses either the YY stellar evolution models (Demarque et al. 2004) or the empirical Torres relations (Torres et al. 2010). Each photometric observation's raw light curve and the detrending parameters determined from the light curve are inputs for the final fit. We impose a prior on $T_{\rm eff}$ and [Fe/H] using the determined values and errors from the SME analysis of the AAT spectra. From analysis of the KELT-South and follow-up photometric observations, we set a prior on the period. For both KELT-14b and KELT-15b, we perform four global fits: (1) Using the YY stellar models with eccentricity fixed at zero. (2) Using the YY stellar models with eccentricity as a free parameter. (3) Using the empirical Torres relations with eccentricity fixed at zero. (4) Using the empirical Torres relations with eccentricity as a free parameter. The results from these four global fits can be seen in Table 7 for the KELT-14 system and Table 8 for the KELT-15 system. For the parameters shown in solar or Jovian units, the values for these constants are $G \ M_\odot = 1.3271244 \times 10^{20}$ m^3 s^{-2}, $R_\odot = 6.9566 \times 10^8$ m, $M_{\rm J} = 0.000954638698 \ M_\odot$, and $R_{\rm J} = 0.102792236 \ R_\odot$ (Standish 1995; Torres et al. 2010; Eastman et al. 2013). All determined values for the four separate global fits are consistent with each other (within 1σ). We adopt the YY circular fit for all analysis and interpretation for KELT-14b and KELT-15b.

4.2. Transit Timing Variation Analysis

We were careful to confirm all observation times are in the BJD_TBD format (Eastman et al. 2010). All time conversions to BJD_TBD were performed in the AIJ reduction using the timestamps in the image headers. The observatory clocks from our follow-up observers are synchronised at the start of each observing session to a standard clock (atomic clock in Boulder, CO for PEST observatory) and typically the synchronization is redone through out the observing night. From our experience, we have found the time stamp in the image header and the actual start of observations can differ by a few seconds. Using only the transit timing data shown in Table 9 and Figure 9, we determined a separate ephemeris from our global fit for

Table 7
Median Values and 68% Confidence Interval for the Physical and Orbital Parameters of the KELT-14 System

Parameter	Units	Adopted Value (YY circular)	Value (YY eccentric)	Value (Torres circular)	Value (Torres eccentric)
Stellar Parameters					
M_*	Mass ($M_\odot$)	$1.178^{+0.052}_{-0.066}$	$1.177^{+0.059}_{-0.066}$	$1.202^{+0.064}_{-0.062}$	$1.203^{+0.066}_{-0.063}$
R_*	Radius ($R_\odot$)	$1.368^{+0.078}_{-0.077}$	$1.378^{+0.10}_{-0.099}$	1.410 ± 0.077	$1.418^{+0.096}_{-0.094}$
L_*	Luminosity ($L_\odot$)	$1.90^{+0.28}_{-0.24}$	$1.93^{+0.34}_{-0.29}$	$2.04^{+0.29}_{-0.26}$	$2.06^{+0.34}_{-0.30}$
ρ_*	Density (cgs)	$0.645^{+0.11}_{-0.087}$	$0.63^{+0.14}_{-0.11}$	$0.604^{+0.096}_{-0.078}$	$0.595^{+0.12}_{-0.094}$
$\log g_*$	Surface gravity (cgs)	$4.234^{+0.045}_{-0.041}$	$4.228^{+0.057}_{-0.054}$	$4.219^{+0.041}_{-0.038}$	$4.215^{+0.051}_{-0.048}$
$T_{\rm eff}$	Effective temperature (K)	5802^{+95}_{-92}	5800^{+96}_{-92}	5815 ± 88	5815 ± 89
[Fe/H]	Metallicity	$0.326^{+0.091}_{-0.089}$	$0.324^{+0.092}_{-0.089}$	$0.338^{+0.087}_{-0.085}$	$0.338^{+0.086}_{-0.085}$
Planet Parameters					
e	Eccentricity	⋯	$0.041^{+0.036}_{-0.027}$	⋯	$0.039^{+0.034}_{-0.026}$
ω_*	Argument of periastron (°)	⋯	149^{+77}_{-65}	⋯	156^{+73}_{-69}
P	Period (days)	$1.7100596^{+0.0000074}_{-0.0000075}$	1.7100597 ± 0.0000074	$1.7100596^{+0.0000074}_{-0.0000073}$	1.7100596 ± 0.0000074
a	Semimajor axis (au)	$0.02956^{+0.00043}_{-0.00057}$	$0.02955^{+0.00048}_{-0.00057}$	0.02976 ± 0.00052	0.02977 ± 0.00053
M_P	Mass (M_j)	1.196 ± 0.072	$1.206^{+0.079}_{-0.076}$	$1.217^{+0.075}_{-0.073}$	$1.226^{+0.081}_{-0.078}$
R_P	Radius (R_j)	$1.52^{+0.12}_{-0.11}$	1.53 ± 0.14	$1.57^{+0.12}_{-0.11}$	$1.57^{+0.14}_{-0.13}$
ρ_P	Density (cgs)	$0.421^{+0.11}_{-0.083}$	$0.414^{+0.12}_{-0.091}$	$0.393^{+0.095}_{-0.076}$	$0.390^{+0.11}_{-0.082}$
$\log g_P$	Surface gravity	$3.107^{+0.066}_{-0.064}$	$3.103^{+0.075}_{-0.071}$	3.089 ± 0.062	$3.088^{+0.068}_{-0.067}$
$T_{\rm eq}$	Equilibrium temperature (K)	1904 ± 54	1910^{+68}_{-67}	1929^{+55}_{-56}	1934 ± 65
$\langle F \rangle$	Incident flux (10^9 erg s^{-1} cm^{-2})	$2.98^{+0.36}_{-0.33}$	$3.02^{+0.45}_{-0.40}$	$3.15^{+0.38}_{-0.35}$	$3.17^{+0.45}_{-0.41}$
RV Parameters					
T_C	Time of inferior conjunction (BJD$_{\rm TDB}$)	2457111.5484 ± 0.0050	2457111.5497 ± 0.0052	$2457111.5485^{+0.0049}_{-0.0050}$	2457111.5496 ± 0.0051
T_P	Time of periastron (BJD$_{\rm TDB}$)	⋯	$2457111.81^{+0.36}_{-0.29}$	⋯	$2457111.84^{+0.35}_{-0.31}$
K	RV semi-amplitude (m s^{-1})	179.8 ± 9.0	181.3 ± 9.3	179.7 ± 8.9	181.2 ± 9.2
$M_P \sin i$	Minimum mass (M_j)	$1.177^{+0.071}_{-0.070}$	$1.185^{+0.076}_{-0.074}$	$1.196^{+0.073}_{-0.072}$ and $1.204^{+0.078}_{-0.075}$	⋯
M_P/M_*	Mass ratio	$0.000974^{+0.000052}_{-0.000051}$	$0.000981^{+0.000053}_{-0.000052}$	$0.000967^{+0.000051}_{-0.000050}$	0.000973 ± 0.000052
u	RM linear limb darkening	0.668 ± 0.011	0.668 ± 0.011	0.668 ± 0.011	0.668 ± 0.011
$\gamma_{\rm AAT}$	m s^{-1}	$34590.0^{+6.8}_{-6.7}$	34590.3 ± 6.7	34590.0 ± 6.7	34590.3 ± 6.6
$\dot\gamma$	RV slope (m s^{-1} day^{-1})	0.53 ± 0.20	0.52 ± 0.23	0.52 ± 0.20	0.53 ± 0.22
$e \cos\omega_*$	⋯	⋯	$-0.019^{+0.021}_{-0.028}$	⋯	$-0.018^{+0.020}_{-0.028}$
$e \sin\omega_*$	⋯	⋯	$0.005^{+0.045}_{-0.033}$	⋯	$0.003^{+0.040}_{-0.032}$
Primary Transit					
R_P/R_*	Radius of the planet in stellar radii	$0.1143^{+0.0029}_{-0.0026}$	$0.1142^{+0.0029}_{-0.0026}$	$0.1141^{+0.0029}_{-0.0026}$	$0.1141^{+0.0030}_{-0.0026}$
a/R_*	Semimajor axis in stellar radii	$4.64^{+0.25}_{-0.22}$	$4.60^{+0.33}_{-0.28}$	$4.54^{+0.23}_{-0.20}$	$4.51^{+0.28}_{-0.25}$
i	Inclination (°)	$79.67^{+0.80}_{-0.77}$	79.5 ± 1.2	79.36 ± 0.75	79.2 ± 1.1
b	Impact parameter	$0.831^{+0.020}_{-0.022}$	$0.831^{+0.020}_{-0.022}$	$0.838^{+0.018}_{-0.020}$	$0.837^{+0.019}_{-0.021}$
δ	Transit depth	$0.01306^{+0.00067}_{-0.00059}$	$0.01305^{+0.00067}_{-0.00059}$	$0.01302^{+0.00067}_{-0.00058}$	$0.01301^{+0.00068}_{-0.00058}$
T_O	Ephemeris from transits (BJD$_{\rm TDB}$)	$2457091.028632 \pm 0.00047$	⋯	⋯	⋯
$P_{\rm Transits}$	Ephemeris period from transits (days)	1.7100588 ± 0.0000025	⋯	⋯	⋯
$T_{\rm FWHM}$	FWHM duration (days)	$0.0626^{+0.0018}_{-0.0025}$	$0.0626^{+0.0017}_{-0.0025}$	$0.0625^{+0.0019}_{-0.0028}$	$0.0625^{+0.0019}_{-0.0028}$
τ	Ingress/egress duration (days)	$0.0262^{+0.0046}_{-0.0037}$	$0.0261^{+0.0046}_{-0.0036}$	$0.0274^{+0.0048}_{-0.0037}$	$0.0274^{+0.0049}_{-0.0037}$
T_{14}	Total duration (days)	$0.0889^{+0.0025}_{-0.0026}$	0.0888 ± 0.0026	$0.0900^{+0.0024}_{-0.0025}$	0.0900 ± 0.0025
P_T	A priori non-grazing transit probability	$0.1910^{+0.0089}_{-0.0094}$	$0.194^{+0.020}_{-0.017}$	$0.1952^{+0.0086}_{-0.0089}$	$0.197^{+0.018}_{-0.016}$
$P_{T,G}$	A priori transit probability	$0.240^{+0.012}_{-0.013}$	$0.244^{+0.025}_{-0.022}$	0.246 ± 0.012	$0.248^{+0.023}_{-0.021}$
u_{1B}	Linear Limb-darkening	0.685 ± 0.026	$0.685^{+0.027}_{-0.026}$	$0.684^{+0.026}_{-0.025}$	$0.684^{+0.026}_{-0.025}$
u_{2B}	Quadratic Limb-darkening	$0.134^{+0.020}_{-0.021}$	$0.133^{+0.020}_{-0.021}$	0.135 ± 0.020	0.135 ± 0.020
u_{1I}	Linear Limb-darkening	$0.294^{+0.015}_{-0.014}$	0.294 ± 0.015	0.293 ± 0.014	0.292 ± 0.014

Table 7
(Continued)

Parameter	Units	Adopted Value (YY circular)	Value (YY eccentric)	Value (Torres circular)	Value (Torres eccentric)
u_{2I}	Quadratic Limb-darkening	$0.2810^{+0.0074}_{-0.0075}$	0.2810 ± 0.0075	$0.2824^{+0.0070}_{-0.0072}$	$0.2825^{+0.0071}_{-0.0073}$
u_{1R}	Linear Limb-darkening	$0.382^{+0.018}_{-0.017}$	0.382 ± 0.018	$0.380^{+0.018}_{-0.017}$	$0.380^{+0.018}_{-0.017}$
u_{2R}	Quadratic Limb-darkening	$0.2777^{+0.0096}_{-0.010}$	$0.2776^{+0.0098}_{-0.010}$	$0.2789^{+0.0094}_{-0.0098}$	$0.2790^{+0.0093}_{-0.0099}$
$u_{1\,Sloang}$	Linear Limb-darkening	$0.602^{+0.025}_{-0.024}$	$0.602^{+0.026}_{-0.025}$	$0.601^{+0.025}_{-0.024}$	$0.601^{+0.025}_{-0.024}$
$u_{2\,Sloang}$	Quadratic Limb-darkening	$0.188^{+0.017}_{-0.018}$	$0.188^{+0.018}_{-0.019}$	$0.189^{+0.017}_{-0.018}$	$0.189^{+0.017}_{-0.018}$
u_{1V}	Linear Limb-darkening	0.484 ± 0.021	$0.484^{+0.022}_{-0.021}$	$0.483^{+0.021}_{-0.020}$	$0.483^{+0.021}_{-0.020}$
u_{2V}	Quadratic Limb-darkening	$0.247^{+0.013}_{-0.014}$	$0.247^{+0.013}_{-0.014}$	0.248 ± 0.013	$0.248^{+0.013}_{-0.014}$
Secondary Eclipse					
T_S	Time of eclipse (BJD$_{TDB}$)	2457110.6934 ± 0.0050	$2457112.384^{+0.022}_{-0.029}$	$2457110.6935^{+0.0049}_{-0.0050}$	$2457112.384^{+0.022}_{-0.029}$
b_S	Impact parameter	⋯	$0.842^{+0.080}_{-0.063}$	⋯	$0.845^{+0.071}_{-0.059}$
$T_{S,FWHM}$	FWHM duration (days)	⋯	$0.0609^{+0.0065}_{-0.019}$	⋯	$0.0612^{+0.0069}_{-0.019}$
τ_S	Ingress/egress duration (days)	⋯	$0.0275^{+0.013}_{-0.0071}$	⋯	$0.0286^{+0.013}_{-0.0071}$
$T_{S,14}$	Total duration (days)	⋯	$0.0872^{+0.0035}_{-0.0048}$	⋯	$0.0887^{+0.0034}_{-0.0045}$
P_S	A priori non-grazing eclipse probability	⋯	$0.1910^{+0.0091}_{-0.0094}$	⋯	$0.1953^{+0.0088}_{-0.0090}$
$P_{S,G}$	A priori eclipse probability	⋯	0.240 ± 0.013	⋯	0.246 ± 0.012

KELT-14b. To determine an independent ephemeris, we performed a linear fit to the transit center times inferred from the global fit for each follow-up observation. With a χ^2 of 26.9 and 6 degrees of freedom, we get $T_0 = 2457091.028632 \pm 0.00046884453$ (BJD$_{TDB}$) and a period of 1.7100588 ± 0.00000247 days. The high χ^2 is likely caused by systematics in the follow-up photometric observations. Although most epochs are consistent with the linear ephemeris listed (see Figure 9), we do have a few apparent outliers (<10 minutes). Significant differences in measured transit times can be a result of the differences in the observatory clocks, observing procedures and conditions, and astrophysical red noise (Carter & Winn 2009). We do not see these outliers as significant. The high χ^2 is likely dominated by the three transits at epoch −1, and specifically the ICO transit which differs from the PEST and Hazelwood transits by 8 minutes. However, we find no evidence of an issue with the observations time stamps and attribute the discrepancy to be a systematic and not astrophysical in nature. Therefore, we are unwilling to claim convincing evidence for significant transit timing variations for KELT-14b. With only three transits of KELT-15b, we do not attempt a TTV analysis.

5. FALSE POSITIVE ANALYSIS

A signal similar to a true planetary event can be created by a variety of astrophysical and non-astrophysical scenarios. As mentioned in Section 2.3.2, we find no correlation between the bisector spans and the measured radial velocities (see Figure 6). All transit depths across optical band passes are consistent and the global fit $\log g_*$ is consistent with the spectroscopic analysis for KELT-14. There is some discrepancy in the KELT-15 $\log g_*$ from the global fit and SME analysis but this is because the AAT spectra do not include the gravity-sensitive MgB triplet to provide a better constraint on $\log g_*$. All spectroscopic observations of both KELT-14 and KELT-15 were thoroughly investigated to ensure that the observed signal arises from the

target star. There are no signs of multiple sets of absorption lines, and no evidence of a blended object with a similar flux as compared to the target star. Combining the agreement of $\log g_*$ from the global fit and SME analysis with the analysis of the stellar spectra, we can rule out all but nearby faint blended companions. Therefore, we are confident that our measured radii (see Tables 7 and 8) are not significantly underestimated. Overall, we find no evidence that KELT-14b and KELT-15b are anything other than transiting exoplanets, but a better estimate of the $\log g_*$ of KELT-15 using a high-resolution spectrum covering the gravity sensitive MgB triplet would help support the planetary nature of the companion.

We also explored the possibility of searching for line of sight companions by comparing photographic plates from the Palomar Observatory Sky Survey over the past ∼50 years (Reid et al. 1991). Unfortunately, the proper motions of KELT-14b and KELT-15b over the last 50 years are too small (<1″) to allow us to search for the presence of background stars or place limits on line of sight companions. Future adaptive optics imaging of both systems would detect the presence of any nearby faint companions, allowing us to measure any flux contamination and better constrain the planetary parameters.

6. DISCUSSION

6.1. Evolution

As can be seen from the results of the global fit (Tables 7 and 8), KELT-14b and KELT-15b are highly inflated planets, joining the ranks of other hot Jupiters that manifest radii much larger than predicted by standard, non-irradiated models. Several authors (e.g., Demory & Seager 2011) have suggested an empirical insolation threshold ($\approx 2 \times 10^8$ erg s^{-1} cm^{-2}) above which hot Jupiters exhibit increasing amounts of radius inflation. KELT-14b and KELT-15b clearly lie above this threshold, with a current estimated insolation of $2.98^{+0.36}_{-0.33} \times 10^9$ erg s^{-1} cm^{-2} and $1.652^{+0.19}_{-0.100} \times 10^9$ erg s^{-1} cm^{-2}, respectively, from the

Table 8
Median Values and 68% Confidence Interval for the Physical and Orbital Parameters of the KELT-15 System

Parameter	Units	Adopted Value (YY circular)	Value (YY eccentric)	Value (Torres circular)	Value (Torres eccentric)
Stellar Parameters					
M_*	Mass ($M_\odot$)	$1.181^{+0.051}_{-0.050}$	$1.218^{+0.10}_{-0.071}$	$1.216^{+0.057}_{-0.055}$	$1.244^{+0.092}_{-0.074}$
R_*	Radius ($R_\odot$)	$1.481^{+0.091}_{-0.041}$	$1.63^{+0.30}_{-0.18}$	$1.493^{+0.082}_{-0.042}$	$1.60^{+0.34}_{-0.17}$
L_*	Luminosity ($L_\odot$)	$2.58^{+0.35}_{-0.20}$	$3.11^{+1.3}_{-0.69}$	$2.65^{+0.32}_{-0.20}$	$3.04^{+1.4}_{-0.65}$
ρ_*	Density (cgs)	$0.514^{+0.034}_{-0.076}$	$0.40^{+0.15}_{-0.14}$	$0.518^{+0.032}_{-0.071}$	$0.42^{+0.15}_{-0.17}$
$\log g_*$	Surface gravity (cgs)	$4.168^{+0.019}_{-0.044}$	$4.100^{+0.086}_{-0.11}$	$4.174^{+0.018}_{-0.040}$	$4.120^{+0.084}_{-0.14}$
$T_{\rm eff}$	Effective temperature (K)	6003^{+56}_{-52}	6017^{+58}_{-57}	6021^{+60}_{-61}	6021^{+61}_{-60}
[Fe/H]	Metallicity	0.047 ± 0.032	$0.051^{+0.033}_{-0.032}$	$0.051^{+0.034}_{-0.033}$	0.051 ± 0.033
Planet Parameters					
e	Eccentricity	⋯	$0.132^{+0.13}_{-0.090}$	⋯	$0.133^{+0.14}_{-0.091}$
ω_*	Argument of periastron (°)	⋯	141^{+71}_{-42}	⋯	142^{+76}_{-42}
P	Period (days)	3.329441 ± 0.000016	3.329442 ± 0.000016	3.329441 ± 0.000016	3.329442 ± 0.000016
a	Semimajor axis (au)	0.04613 ± 0.00065	$0.04660^{+0.0013}_{-0.00092}$	0.04657 ± 0.00072	$0.04693^{+0.0011}_{-0.00095}$
M_P	Mass (M_j)	$0.91^{+0.21}_{-0.22}$	$0.94^{+0.26}_{-0.25}$	0.93 ± 0.22	$0.95^{+0.26}_{-0.25}$
R_P	Radius (R_j)	$1.443^{+0.11}_{-0.057}$	$1.59^{+0.31}_{-0.19}$	$1.453^{+0.098}_{-0.057}$	$1.56^{+0.34}_{-0.18}$
ρ_P	Density (cgs)	$0.36^{+0.11}_{-0.10}$	$0.28^{+0.15}_{-0.11}$	$0.363^{+0.11}_{-0.100}$	$0.29^{+0.16}_{-0.13}$
$\log g_P$	Surface gravity	$3.02^{+0.10}_{-0.13}$	$2.95^{+0.14}_{-0.17}$	$3.03^{+0.10}_{-0.12}$	$2.96^{+0.15}_{-0.18}$
$T_{\rm eq}$	Equilibrium temperature (K)	1642^{+45}_{-25}	1713^{+140}_{-92}	1645^{+41}_{-25}	1699^{+150}_{-87}
$\langle F \rangle$	Incident flux (10^9 erg s^{-1} cm^{-2})	$1.652^{+0.19}_{-0.100}$	$1.92^{+0.58}_{-0.37}$	$1.66^{+0.17}_{-0.10}$	$1.86^{+0.63}_{-0.35}$
RV Parameters					
T_C	Time of inferior conjunction (BJD$_{\rm TDB}$)	$2457029.1663^{+0.0078}_{-0.0073}$	$2457029.1691^{+0.0083}_{-0.0081}$	$2457029.1663^{+0.0079}_{-0.0073}$	$2457029.1688^{+0.0084}_{-0.0080}$
T_P	Time of periastron (BJD$_{\rm TDB}$)	⋯	$2457029.49^{+0.64}_{-0.29}$	⋯	$2457029.50^{+0.71}_{-0.29}$
K	RV semi-amplitude (m s^{-1})	110 ± 26	113 ± 30	110 ± 26	113^{+30}_{-29}
$M_P \sin i$	Minimum mass (M_j)	$0.91^{+0.21}_{-0.22}$	$0.94^{+0.26}_{-0.25}$	0.93 ± 0.22	$0.95^{+0.26}_{-0.25}$
M_P/M_*	Mass ratio	0.00073 ± 0.00017	0.00073 ± 0.00019	0.00073 ± 0.00017	0.00073 ± 0.00019
u	RM linear limb darkening	$0.6290^{+0.0062}_{-0.0058}$	$0.6275^{+0.0065}_{-0.0059}$	$0.6276^{+0.0066}_{-0.0074}$	$0.6272^{+0.0066}_{-0.0060}$
$\gamma_{\rm AAT}$	m s^{-1}	12204^{+18}_{-19}	12203 ± 21	12204 ± 19	12204 ± 20
$\gamma_{\rm CORALIE}$	m s^{-1}	12216 ± 22	12212 ± 22	12216 ± 21	12211 ± 22
$e \cos \omega_*$	⋯	⋯	$-0.073^{+0.073}_{-0.10}$	⋯	$-0.074^{+0.074}_{-0.10}$
$e \sin \omega_*$	⋯	⋯	$0.050^{+0.14}_{-0.082}$	⋯	$0.042^{+0.16}_{-0.085}$
Primary Transit					
R_P/R_*	Radius of the planet in stellar radii	$0.1001^{+0.0022}_{-0.0021}$	$0.1005^{+0.0025}_{-0.0023}$	$0.1001^{+0.0021}_{-0.0020}$	$0.1001^{+0.0022}_{-0.0021}$
a/R_*	Semimajor axis in stellar radii	$6.70^{+0.14}_{-0.35}$	$6.16^{+0.68}_{-0.83}$	$6.72^{+0.13}_{-0.32}$	$6.29^{+0.67}_{-0.99}$
i	Inclination (°)	$88.3^{+1.2}_{-1.7}$	$87.8^{+1.6}_{-2.3}$	$88.4^{+1.1}_{-1.6}$	$88.1^{+1.3}_{-2.2}$
b	Impact parameter	$0.20^{+0.18}_{-0.14}$	$0.22^{+0.19}_{-0.15}$	$0.19^{+0.17}_{-0.13}$	$0.20^{+0.17}_{-0.13}$
δ	Transit depth	$0.01003^{+0.00044}_{-0.00041}$	$0.01009^{+0.00050}_{-0.00041}$	$0.01001^{+0.00043}_{-0.00041}$	$0.01002^{+0.00044}_{-0.00041}$
$T_{\rm FWHM}$	FWHM duration (days)	$0.1552^{+0.0015}_{-0.0016}$	$0.1552^{+0.0017}_{-0.0018}$	$0.1551^{+0.0015}_{-0.0016}$	0.1550 ± 0.0016
τ	Ingress/egress duration (days)	$0.01635^{+0.0021}_{-0.00079}$	$0.01656^{+0.0026}_{-0.00093}$	$0.01627^{+0.0019}_{-0.00074}$	$0.01631^{+0.0020}_{-0.00076}$
T_{14}	Total duration (days)	$0.1719^{+0.0025}_{-0.0021}$	$0.1722^{+0.0030}_{-0.0024}$	$0.1717^{+0.0024}_{-0.0020}$	$0.1717^{+0.0025}_{-0.0021}$
P_T	A priori non-grazing transit probability	$0.1343^{+0.0072}_{-0.0027}$	$0.155^{+0.058}_{-0.026}$	$0.1340^{+0.0066}_{-0.0026}$	$0.151^{+0.068}_{-0.025}$
$P_{T,G}$	A priori transit probability	$0.1642^{+0.0092}_{-0.0036}$	$0.190^{+0.070}_{-0.032}$	$0.1637^{+0.0084}_{-0.0033}$	$0.185^{+0.084}_{-0.031}$
u_{1I}	Linear Limb-darkening	$0.2500^{+0.0078}_{-0.0069}$	$0.2471^{+0.0086}_{-0.0079}$	$0.2482^{+0.0083}_{-0.0073}$	$0.2468^{+0.0086}_{-0.0077}$
u_{2I}	Quadratic Limb-darkening	$0.2964^{+0.0027}_{-0.0036}$	$0.2980^{+0.0036}_{-0.0040}$	$0.2972^{+0.0028}_{-0.0037}$	$0.2980^{+0.0034}_{-0.0039}$
u_{1R}	Linear Limb-darkening	$0.3259^{+0.0092}_{-0.0080}$	$0.3231^{+0.0098}_{-0.0086}$	$0.3237^{+0.0098}_{-0.0083}$	$0.3227^{+0.0098}_{-0.0085}$
u_{2R}	Quadratic Limb-darkening	$0.3027^{+0.0033}_{-0.0046}$	$0.3042^{+0.0038}_{-0.0048}$	$0.3037^{+0.0035}_{-0.0048}$	$0.3043^{+0.0037}_{-0.0048}$
u_{1V}	Linear Limb-darkening	$0.4158^{+0.011}_{-0.0091}$	$0.4132^{+0.011}_{-0.0092}$	$0.4133^{+0.011}_{-0.0094}$	$0.4127^{+0.011}_{-0.0094}$
u_{2V}	Quadratic Limb-darkening	$0.2858^{+0.0045}_{-0.0061}$	$0.2871^{+0.0044}_{-0.0061}$	$0.2871^{+0.0046}_{-0.0062}$	$0.2874^{+0.0045}_{-0.0061}$
Secondary Eclipse					
T_S	Time of eclipse (BJD$_{\rm TDB}$)	$2457027.5016^{+0.0078}_{-0.0073}$	$2457030.68^{+0.16}_{-0.22}$	$2457027.5015^{+0.0079}_{-0.0073}$	$2457030.68^{+0.16}_{-0.22}$
b_S	Impact parameter	⋯	$0.25^{+0.22}_{-0.17}$	⋯	$0.22^{+0.22}_{-0.15}$
$T_{S,\rm FWHM}$	FWHM duration (days)	⋯	$0.168^{+0.046}_{-0.022}$	⋯	$0.166^{+0.052}_{-0.024}$

Table 8
(Continued)

Parameter	Units	Adopted Value (YY circular)	Value (YY eccentric)	Value (Torres circular)	Value (Torres eccentric)
τ_S	Ingress/egress duration (days)	⋯	$0.0193^{+0.0076}_{-0.0039}$	⋯	$0.0185^{+0.0085}_{-0.0036}$
$T_{S,14}$	Total duration (days)	⋯	$0.189^{+0.051}_{-0.026}$	⋯	$0.186^{+0.060}_{-0.028}$
P_S	A priori non-grazing eclipse probability	⋯	$0.1394^{+0.011}_{-0.0057}$	⋯	$0.1383^{+0.011}_{-0.0051}$
$P_{S,G}$	A priori eclipse probability	⋯	$0.1705^{+0.014}_{-0.0072}$	⋯	$0.1690^{+0.014}_{-0.0064}$

Table 9
Transit Times for KELT-14b

Epoch	T_C (BJD$_{\mathrm{TDB}}$)	σ_{T_C} (s)	O–C (s)	O–C (σ_{T_C})	Telescope
−29	2457043.146899	67	−5.00	−0.07	PEST
−26	2457048.276707	83	−37.99	−0.45	PEST
−1	2457091.027548	93	−102.01	−1.09	PEST
−1	2457091.033997	134	455.19	3.37	ICO
−1	2457091.027674	121	−91.12	−0.75	Hazelwood
6	2457103.002776	119	311.42	2.60	Hazelwood
11	2457111.550157	169	57.80	0.34	LCOGT
13	2457114.965950	113	−316.62	−2.78	Hazelwood
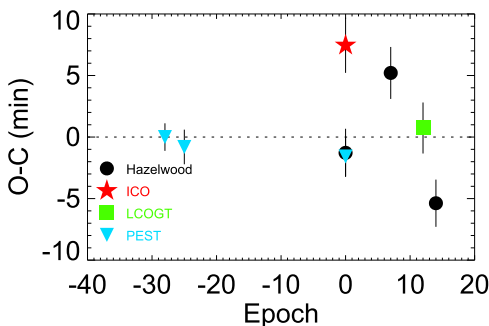
Figure 9. Transit time residuals for KELT-14b using our final global fit ephemeris. The times are listed in Table 9.

global fits, and therefore their currently large inflated radii are not surprising. At the same time, the KELT-14 and KELT-15 host stars are both found to be at present in a state of evolution wherein the stellar radii are expanding as the stars prepare to cross the Hertzsprung gap toward the red giant branch. This means that the stars' surfaces are encroaching on their planets, which presumably is in turn driving up the planets' insolations and also the rate of any tidal interactions between the planets and the stars.

Therefore it is interesting to consider two questions. First, has KELT-14b's and KELT-15b's incident radiation from their host stars been below the empirical radius inflation threshold in the past? If either planet's insolation only recently exceeded the inflation threshold, the system could then serve as an empirical test bed for the different timescales predicted by different inflation mechanisms (see, e.g., Assef et al. 2009; Spiegel & Madhusudhan 2012). Second, what is the expected fate of the KELT-14b and KELT-15b planets given the increasingly strong tidal interactions they are experiencing with their encroaching host stars?

To investigate these questions, we follow Penev et al. (2014) to simulate the reverse and forward evolution of the star-planet system, using the measured parameters listed in Tables 7 and 8

as the present-day boundary conditions. This analysis is not intended to examine any type of planet–planet or planet–disk migration effects. Rather, it is a way to investigate (1) the change in insolation of the planet over time due to the changing luminosity of the star and changing star-planet separation, and (2) the change in the planet's orbital semimajor axis due to the changing tidal torque as the star-planet separation changes with the evolving stellar radius. We include the evolution of the star, assumed to follow the YY stellar model with mass and metallicity. For simplicity we assume that the stellar rotation is negligible and treat the star as a solid body. We also assume a circular orbit aligned with the stellar equator throughout the analysis. The results of our simulations are shown in Figure 10. We tested a range of values for the tidal quality factor of the star divided by the love number, $Q'_\star \equiv Q_\star/k_2$, from $\log Q'_\star = 5$ to $\log Q'_\star = 7$ (assuming a constant phase lag between the tidal bulge and the star-planet direction).

We find that although for certain values of $Q'_\star$ the planets may have been initially below the insolation inflation threshold during the first ~100 Myr, in all cases the planets have always received more than enough flux from their hosts to keep the planets irradiated beyond the insolation threshold identified by Demory & Seager (2011).

KELT-15b appears destined to survive for at least the next few Gyr, unless the stellar $Q'_\star$ is very small, in which case it is predicted to experience a rapid in-spiral into its host star. In the case of KELT-14b, the current evolution of the star suggests a concomitant in-spiral of the planet over the next ~1 Gyr, and even faster if the stellar $Q'_\star$ is small. This planet therefore does not appear destined to survive beyond the star's subgiant phase. As additional systems like KELT-14b are discovered and their evolution investigated in detail, it will be interesting to examine the statistics of planet survival and to compare these to predictions such as those shown here in Figure 10 to constrain mechanisms of planet-star interaction generally and the values of $Q'_\star$ specifically.

6.2. Opportunities for Atmospheric Characterization

Because of its very high equilibrium temperature (1904 K) and its bright K-band magnitude ($K = 9.424$), KELT-14b is an excellent target for detailed atmospheric characterization. Specifically we note that it is an especially ideal target for eclipse observations. Measurements during the secondary eclipse of a hot Jupiter provide a direct measurement of thermal emission from the planet's dayside and allow constraints on the connection between the atmospheric structure and climate and irradiation from the host star. As illustrated in Figure 11, KELT-14b has the second largest expected emission signal in the K-band for known transiting planets brighter than $K < 10.5$. We therefore encourage follow up of this planet in eclipse in order to aid comparative studies
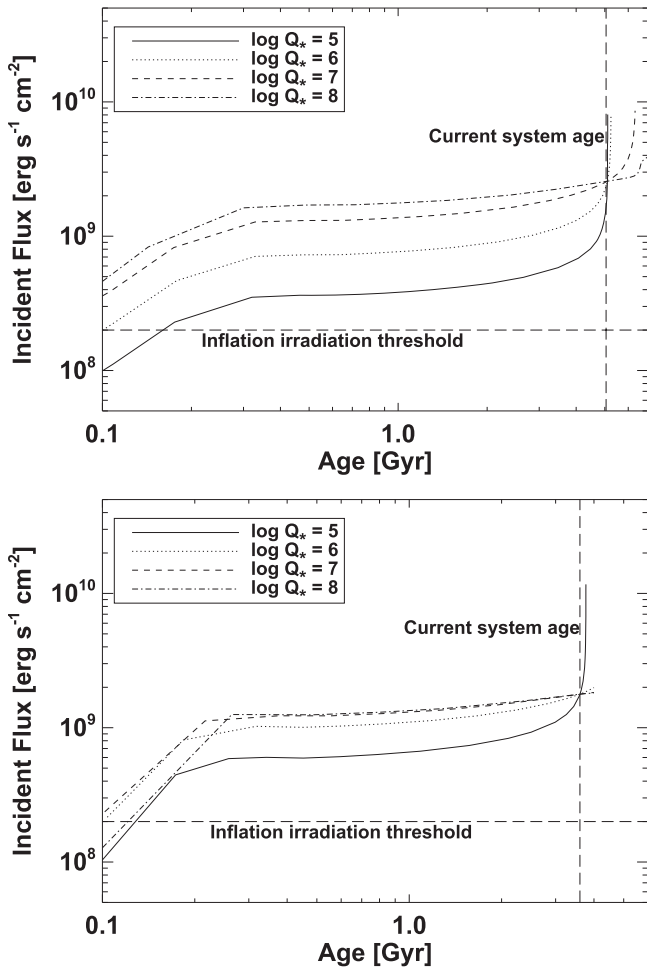
Figure 10. The inflation irradiation history for (top) KELT-14 and (bottom) KELT-15 shown for test values of $\log Q_*'$ of 5–8. The model assumes the stellar rotation is negligible and treats the star as a solid body. Also the model assumes a circular orbit aligned with the stellar equator. For both KELT-14b and KELT-15b, we find an the insolation received is above the empirical threshold (horizontal dashed line) determined by Demory & Seager (2011). The vertical line represents the estimated current age of the system.

Figure 11. The expected day-side thermal emission from the planet in the K-band (assuming no redistribution of heat) for all known transiting planets brighter than a K-band magnitude of 11. Along with KELT-14b and KELT-15b, we highlight WASP-33b, one of the hottest known transiting planets and KELT-7b, another very hot and very bright planet discovered by the northern component of the KELT survey. Data are from this paper and the NASA Exoplanet Archive, accessed on 2015 August 27.

14 to characterize the long term trend we observed. Also, the Rossiter–McLaughlin (R–M) signal for both KELT-14b and KELT-15b should be detectable with current ground-based facilities. (The expected R–M semi-amplitude for both is $\sim 90\,\mathrm{m\,s}^{-1}$.) Two of the RV observations of KELT-15b were taken during the transit and hint at a prograde orbit. However, due to the limited data acquired in transit, we do not claim KELT-15b to be in a prograde orbit but suggest future R–M observations to determine the spin–orbit alignment of the system.

7. SUMMARY AND CONCLUSIONS

We present the discovery of two more transiting inflated hot Jupiter exoplanets from the KELT-South survey, KELT-14b and KELT-15b. KELT-14b, the independent discovery of WASP-122b (Turner et al. 2015) has a period of $1.7100596^{+0.0000074}_{-0.0000075}$ days, a radius of $1.52^{+0.12}_{-0.11}\,R_J$ and a mass of $1.196 \pm 0.072\,M_J$. KELT-15b has a period of 3.329441 ± 0.000016 days, a radius of $1.443^{+0.11}_{-0.057}\,R_J$ and a mass of $0.91^{+0.21}_{-0.22}\,M_J$. Additional follow-up transits are highly desirable for KELT-15b in order to better refine the ephemeris for future follow-up studies. Both KELT-14b and KELT-15b orbit host stars that are bright in the near-IR ($K = 9.424$ and 9.854, respectively), making them attractive targets for atmospheric characterization through secondary eclipse observations. Both should have large enough emission signals that they can be observed using ground-based observatories. These newly discovered planets increase the number of targets suitable for atmospheric characterization in the southern hemisphere.

of exoplanet atmospheres and better understand the connection between irradiation, albedo, and atmospheric circulation.

With an equilibrium temperature of 1642 K, KELT-15b is not as hot as KELT-14b. However, it still has a comparably large expected emission signal in the K band that should be detectable with ground-based telescopes. Observing multiple planets in eclipse that span a range of temperatures and other properties is particularly useful for comparative exoplanetology.

6.3. Spectroscopic Follow-up

From the global fit, we find that KELT-14b has an RV slope of $0.53 \pm 0.20\,\mathrm{m\,s}^{-1}\,\mathrm{day}^{-1}$. It is possible that this RV trend is a result of a tertiary component in the system. Another discovery from the KELT survey, KELT-6b, showed an RV slope of $-0.239 \pm 0.037\,\mathrm{m\,s}^{-1}\,\mathrm{day}^{-1}$ (Collins et al. 2014), which was recently confirmed to be the result of KELT-6c, a 3.5 year period companion with a minimum mass of $M_P \sin i = 3.71 \pm 0.21\,M_J$ (Damasso et al. 2015). We therefore recommend long term spectroscopic follow-up of KELT-

RODRIGUEZ ET AL.

REFERENCES

Addison, B. C., Tinney, C. G., Wright, D. J., et al. 2013, ApJL, 774, L9
Addison, B. C., Tinney, C. G., Wright, D. J., & Bayliss, D. 2014, ApJ, 792, 112
Alonso, R., Brown, T. M., Torres, G., et al. 2004, ApJL, 613, L153
Ammons, S. M., Robinson, S. E., Strader, J., et al. 2006, ApJ, 638, 1004
Assef, R. J., Gaudi, B. S., & Stanek, K. Z. 2009, ApJ, 701, 1616
Baglin, A., Auvergne, M., Boisnard, L., et al. 2006, in COSPAR Meeting 36, 36th COSPAR Scientific Assembly, 3749
Bakos, G., Noyes, R. W., Kovács, G., et al. 2004, PASP, 116, 266
Baranne, A., Queloz, D., Mayor, M., et al. 1996, A&AS, 119, 373
Bayliss, D., Zhou, G., Penev, K., et al. 2013, AJ, 146, 113
Beatty, T. G., Pepper, J., Siverd, R. J., et al. 2012, ApJL, 756, L39
Bensby, T., Feltzing, S., & Lundström, I. 2003, A&A, 410, 527
Bieryla, A., Collins, K., Beatty, T. G., et al. 2015, AJ, 150, 12
Borucki, W. J., Koch, D., Basri, G., et al. 2010, Sci, 327, 977
Carter, J. A., & Winn, J. N. 2009, ApJ, 704, 51
Castelli, F., & Kurucz, R. L. 2004, arXiv:astro-ph/0405087
Cloutier, R., & Lin, M.-K. 2013, MNRAS, 434, 621
Coşkunoğlu, B., Ak, S., Bilir, S., et al. 2011, MNRAS, 412, 1237
Collins, K., & Kielkopf, J. 2013, AstroImageJ: ImageJ for Astronomy, Astrophysics Source Code Library, ascl:1309.001
Collins, K. A. 2015, Electronic Theses and Dissertations, Univ. Louisville
Collins, K. A., Eastman, J. D., Beatty, T. G., et al. 2014, AJ, 147, 39
Cutri, R. M., Skrutskie, M. F., van Dyk, S., et al. 2003, yCat, 2246, 0
Cutri, R. M., Wright, E. L., Conrow, T., et al. 2012, yCat, 2311, 0

Damasso, M., Esposito, M., Nascimbeni, V., et al. 2015, A&A, 581, L6
D'Angelo, G., & Lubow, S. H. 2008, ApJ, 685, 560
Demarque, P., Woo, J.-H., Kim, Y.-C., & Yi, S. K. 2004, ApJS, 155, 667
Demory, B.-O., & Seager, S. 2011, ApJS, 197, 12
Dopita, M., Hart, J., McGregor, P., et al. 2007, Ap&SS, 310, 255
Eastman, J., Gaudi, B. S., & Agol, E. 2013, PASP, 125, 83
Eastman, J., Siverd, R., & Gaudi, B. S. 2010, PASP, 122, 935
Fulton, B. J., Collins, K. A., Gaudi, B. S., et al. 2015, ApJ, 810, 30
Gómez Maqueo Chew, Y., Faedi, F., Cargile, P., et al. 2013, ApJ, 768, 79
Hartman, J. 2012, Astrophysics Source Code Library, ascl:1208.016
Henden, A. A., Levine, S., Terrell, D., & Welch, D. L. 2015, in American Astronomical Society Meeting Abstracts, 225, 33616
Høg, E., Fabricius, C., Makarov, V. V., et al. 2000, A&A, 355, L27
Horton, A., Tinney, C. G., Case, S., et al. 2012, Proc. SPIE, 8446, 3
Hubeny, I., & Lanz, T. 2011, VARTOOLS: Light Curve Analysis Program, Astrophysics Source Code Library, ascl:1109.022
Jackson, B., Greenberg, R., & Barnes, R. 2008, ApJ, 678, 1396
Jensen, E. 2013, Tapir: A web interface for transit/eclipse observability Astrophysics Source Code Library, ascl:1306.007
Kovács, G., Zucker, S., & Mazeh, T. 2002, A&A, 391, 369
Kuhn, R. B., Rodriguez, J. E., Collins, K. A., et al. 2015, arXiv:1509.02323
Martin, D. C., Fanson, J., Schiminovich, D., et al. 2005, ApJL, 619, L1
Masset, F. S., & Papaloizou, J. C. B. 2003, ApJ, 588, 494
McCullough, P. R., Stys, J. E., Valenti, J. A., et al. 2006, ApJ, 648, 1228
Penev, K., Zhang, M., & Jackson, B. 2014, PASP, 126, 553
Pepe, F., Mayor, M., Galland, F., et al. 2002, A&A, 388, 632
Pepper, J., Kuhn, R. B., Siverd, R., James, D., & Stassun, K. 2012, PASP, 124, 230
Pepper, J., Pogge, R. W., DePoy, D. L., et al. 2007, PASP, 119, 923
Pepper, J., Siverd, R. J., Beatty, T. G., et al. 2013, ApJ, 773, 64
Pickles, A., & Depagne, É 2010, PASP, 122, 1437
Pollacco, D. L., Skillen, I., Collier Cameron, A., et al. 2006, PASP, 118, 1407
Queloz, D., Mayor, M., Udry, S., et al. 2001, Msngr, 105, 1
Reid, I. N., Brewer, C., Brucato, R. J., et al. 1991, PASP, 103, 661
Schlegel, D. J., Finkbeiner, D. P., & Davis, M. 1998, ApJ, 500, 525
Siverd, R. J., Beatty, T. G., Pepper, J., et al. 2012, ApJ, 761, 123
Skrutskie, M. F., Cutri, R. M., Stiening, R., et al. 2006, AJ, 131, 1163
Soderblom, D. R. 1983, ApJS, 53, 1
Spiegel, D. S., & Madhusudhan, N. 2012, ApJ, 756, 132
Standish, E. M. 1995, HiA, 10, 180
Tanaka, H., Takeuchi, T., & Ward, W. R. 2002, ApJ, 565, 1257
Torres, G., Andersen, J., & Giménez, A. 2010, A&ARv, 18, 67
Turner, O. D., Anderson, D. R., Collier Cameron, A., et al. 2015, arXiv:1509.02210
Valenti, J. A., & Fischer, D. A. 2005, ApJS, 159, 141
Valenti, J. A., & Piskunov, N. 1996, A&AS, 118, 595
Walsh, K. J., Morbidelli, A., Raymond, S. N., O'Brien, D. P., & Mandell, A. M. 2011, Natur, 475, 206
Wildi, F., Pepe, F., Chazelas, B., Lo Curto, G., & Lovis, C. 2011, Proc. SPIE, 8151, 81511
Wright, E. L., Eisenhardt, P. R. M., Mainzer, A. K., et al. 2010, AJ, 140, 1868
Zacharias, N., Monet, D. G., Levine, S. E., et al. 2004, BAAS, 36, 1418